The Astrophysical Journal, 980:19 (15pp), 2025 February 10 https://doi.org/10.3847/1538-4357/ada3bc

Revisiting the Flaring Activity in Early 2015 of BL Lacertae Object S5 0716+714

Zhihao Ouyang[1,2], Hubing Xiao[1], Marina Manganaro[3], Shangchun Xie[1], Jingyu Wu[1], Jianzhen Chen[1], Rui Xue[4], Gege Wang[5], Shaohua Zhang[1], and Junhui Fan[2,6,7,8]

[1] Shanghai Key Lab for Astrophysics, Shanghai Normal University, Shanghai, 200234, People's Republic of China; hubing.xiao@shnu.edu.cn, jzchen@shnu.edu.cn
[2] Center for Astrophysics, Guangzhou University, Guangzhou, 510006, People's Republic of China
[3] Department of Physics, University of Rijeka, Rijeka, 51000, Croatia; marina.manganaro@phy.uniri.hr
[4] Department of Physics, Zhejiang Normal University, Jinhua, 321004, People's Republic of China
[5] Key Laboratory of Cosmology and Astrophysics (Liaoning) & College of Sciences, Northeastern University, Shenyang, 110819, People's Republic of China
[6] Great Bay Brand Center of the National Astronomical Data Center, Guangzhou, 510006, People's Republic of China
[7] Key Laboratory for Astronomical Observation and Technology of Guangzhou, Guangzhou, 510006, People's Republic of China
[8] Astronomy Science and Technology Research Laboratory of Department of Education of Guangdong Province, Guangzhou, 510006, People's Republic of China
Received 2024 September 12; revised 2024 December 13; accepted 2024 December 27; published 2025 January 31

Abstract

In this work, we analyzed multiwavelength data of the BL Lac object S5 0716+714 to investigate its emission mechanisms during a flaring state observed in early 2015. We examined the temporal behavior and broadband spectral energy distributions (SEDs) during the flare. The size of the γ-ray emission region was estimated based on the variability timescale. To explore the multiwavelength properties of S5 0716+714, we employed three one-zone models: the synchrotron self-Compton (SSC) model, the SSC plus external Compton (EC) model, and the SSC plus *pp* interactions model, to reproduce the SEDs. Our findings indicate that, while the SSC model can describe the SEDs, it requires an extreme Doppler factor. In contrast, the SSC plus EC model successfully fits the SEDs under the assumption of weak external photon fields but requires a high Doppler factor. Additionally, the SSC plus *pp* interactions model also reproduces the SEDs, with γ-ray emission originating from π^0 decay. However, this model leads to a jet power that exceeds the Eddington luminosity, which remains plausible due to the flaring state or the presence of a highly collimated jet.

Unified Astronomy Thesaurus concepts: BL Lacertae objects (158); Blazars (164); Active galactic nuclei (16)

1. Introduction

Blazars, a unique subclass of active galactic nuclei, exhibit extreme observational characteristics including strong variability, high polarization, superluminal motion, and γ-ray radiation (e.g., C. M. Urry & P. Padovani 1995; J.-H. Fan et al. 2004; M. Lyutikov & E. V. Kravchenko 2017; M. L. Lister et al. 2019; H. Xiao et al. 2019; S. Abdollahi et al. 2022; H. B. Xiao et al. 2022, and references therein). Blazars are grouped into two subclasses based on their optical continuum: BL Lacertae objects, which show weak or absent emission lines (equivalent width, EW < 5 Å), and flat spectrum radio quasars, which show prominent emission lines (EW $\geqslant 5$ Å; M. Stickel et al. 1991; C. M. Urry & P. Padovani 1995; R. Scarpa & R. Falomo 1997). The spectral energy distribution (SED) exhibits a distinct two-hump structure. The low-energy hump, observed in the infrared to X-ray range, is attributed to a synchrotron emission of relativistic electrons. The high-energy (HE) hump, located at MeV to GeV energies, can be generated either through the inverse Compton (IC) process in a leptonic scenario (F. Tavecchio et al. 1998; G. Ghisellini & F. Tavecchio 2009; C. Tan et al. 2020) or through a hadronic model (e.g., A. Mücke et al. 2003; M. Böttcher et al. 2009; M. Cerruti et al. 2015, 2019; S. Gao et al. 2019; R. Xue et al. 2022).

S5 0716+714 (4FGL J0721.9+7120) is classified as an intermediate-peak-frequency BL Lacertae object according to J. H. Fan et al. (2016), located at a distance of $z = 0.2304 \pm 0.0013$ (A. Pichel et al. 2023). It was first discovered in the late 1970s in the radio band (R. A. Perley et al. 1980; H. Kuehr et al. 1981), and early radio observations showed strong emission and notable variability (A. Kraus et al. 2003). Subsequent high-resolution very long baseline interferometry (VLBI) observations showed that S5 0716+714's jet components exhibit fast superluminal motion, indicating it has a strong Doppler beaming effect (e.g., U. Bach et al. 2005; B. Rani et al. 2015). Optical observations have been pivotal in studying the variability of S5 0716+714. Previous studies demonstrated rapid variability on timescales of hours to days (S. J. Wagner et al. 1996; H. Poon et al. 2009; A. C. Gupta et al. 2012; T. Tripathi et al. 2024), with intraday variability suggesting a compact emission region for S5 0716+714. Long-term optical monitoring programs have reported a bluer-when-brighter behavior (e.g., B.-z. Dai et al. 2015; D. Xiong et al. 2020). Additionally, Y. Ikejiri et al. (2011) performed the photopolarimetric monitoring observations, revealing complex variability in both the degree and angle of polarization, supporting the hypothesis that the optical emission primarily originates from synchrotron radiation. ROSAT provided the first X-ray detection, and it showed significant rapid variability and a double power-law fitted spectrum, implying a mixture of synchrotron and inverse Compton components in the X-ray band (M. Cappi et al. 1994). More recent X-ray observations have offered detailed spectral and temporal analyses; they showed that the X-ray fluxes were highly variable, and the break energy between the synchrotron and inverse Compton components shifted during different flux states (L. Foschini et al. 2006; A. Wierzcholska & H. Siejkowski 2015, 2016). The source was first detected in the γ-ray band by EGRET on board the Compton Gamma-Ray Observatory and has since been

detected several times at different flux levels (Y. C. Lin et al. 1995; R. C. Hartman et al. 1999). It is one of the brightest and most variable sources in the γ-ray band, with a variability index of 3680.86 reported by the Fermi Large Area Telescope (LAT; S. Abdollahi et al. 2022). Several studies have attempted to explore the γ-ray activity of S5 0716+714. For example, B. Rani et al. (2014) reported a significant correlation between γ-ray fluxes and position angle variations in the VLBI jet, while X. Geng et al. (2020) found a highly variable γ-ray flux with a spectral break between 0.93 and 6.90 GeV through long-term observations. Simultaneously, a multiwavelength observation has been employed as an effective method to study the blazar emission mechanisms. B. Rani et al. (2013a) conducted a comprehensive campaign, including radio, optical, X-ray, and γ-ray observations, to investigate a detailed temporal behavior and constructed a broadband detailed SED. Similarly, N. H. Liao et al. (2014) performed a multiwavelength study of S5 0716+714, finding significant variability and correlation across all bands, and suggesting that the synchrotron self-Compton (SSC) plus external Compton (EC) model is preferred to describe the broadband SED.

The first very-high-energy (VHE) γ-ray detection of S5 0716 +714 was performed by Major Atmospheric Gamma-ray Imaging Cherenkov (MAGIC) telescopes in 2007 (H. Anderhub et al. 2009). In the latter work, the observation gave a significance of 5.8σ over 13.1 hr of observation in 2007 November, and a significance of 6.9σ in 2008 April. Interestingly, the VHE observation coincided with optical high-state emission, implying a possible correlation between VHE and optical emission. This led to the exploration of the one-zone SSC model and the structured ("spine+layer") jet model (H. Anderhub et al. 2009). In late 2014 December, S5 0716+714 became brighter in the optical and infrared bands, exhibiting an exceptionally high state in 2015 January, with the highest flux recorded in these bands (R. Bachev & A. Strigachev 2015; R. Bachev et al. 2015; L. Carrasco et al. 2015). MAGIC observations triggered by this flare revealed a potentially variable VHE flux ranging from 4×10^{-11} to 7×10^{-11} cm^{-2} s^{-1} above 150 GeV between 2015 January 22 and January 26, (R. Mirzoyan 2015; MAGIC Collaboration et al. 2018). This activity was studied in detail in MAGIC Collaboration et al. (2018) based on the multiwavelength observations of its flaring behavior in 2015 January. They stated that, due to the high level of optical flux, the broadband SED of the source cannot be reproduced by a one-zone SSC model. Instead, an interaction between a superluminal knot and a recollimation knot was found, implying a two-zone model was preferred. However, the model underestimates the γ-ray flux in 10 ~ 100 GeV. In addition, the electric vector position angle showed a fast rotation of ~360° and the high-energy γ-ray flare occurring during the γ-ray flaring activity, suggesting a shock–shock interaction in the jet. Considering the polarization variations during the flare, S. Chandra et al. (2015) suggested that the magnetic reconnections were likely involved in this flare. There is no doubt that it is necessary to further study the radiation mechanism of the S5 0716+714 flare that occurred in 2015 January.

In this work, we aim to further explore the high-energy emission of S5 0716+714 during the 2015 January and February flare. We will report on the multiwavelength campaign involving Swift, the Nuclear Spectroscopic Telescope Array (NuSTAR), Fermi, and MAGIC observations, and investigate the temporal behavior and spectral properties of the source. Additionally, we aim to restructure the emission region and reproduce the broadband SED with a new hybrid model.

The paper is structured as follows. The observation introduction and the data reduction are presented in Section 2. The result and discussion are presented in Section 3. Finally, the summary is given in Section 4.

2. Observation and Data Reduction

2.1. Swift Observation

The Neil Gehrels Swift Gamma-Ray Burst Observatory (Swift; N. Gehrels et al. 2004) was launched in 2004 and includes three instruments: the Ultraviolet and Optical Telescope (UVOT; P. W. A. Roming et al. 2005), the X-ray telescope (XRT; D. N. Burrows et al. 2004), and the Burst Alert Telescope (S. D. Barthelmy et al. 2005). The analysis was performed using the HEASoft package (v6.31.1) released by the NASA High Energy Astrophysics Archive Research Center.

2.1.1. Swift-UVOT

The Swift-UVOT observations (P. W. A. Roming et al. 2005) include three optical (v, b, and u) and three UV ($w1$, $m2$, and $w2$) photometric bands (T. S. Poole et al. 2008; A. A. Breeveld et al. 2010). The source region was extracted from a circular region of 5″ centered on the source, and the background region was extracted from a circular region of 20″ near the source for all filters. The `uvotmaghist` task was used to analyze all filter data and produce the photometric light-curve data using the calibration from the release of CALDB (version 20211108). All the UVOT data were checked for the small-scale sensitivity inhomogeneities, which occur when the source falls within the small areas of low sensitivity.[9] In addition, photometric data in which the source was saturated were excluded. Galactic extinction was corrected for the observed magnitude with a value of $E(B-V) = 0.0268$ (E. F. Schlafly & D. P. Finkbeiner 2011) using the interstellar extinction law with $R_V = 3.1$ (E. L. Fitzpatrick 1999). Finally, the corrected magnitudes were converted into fluxes using the standard zero-points from A. A. Breeveld et al. (2011).

2.1.2. Swift-XRT

For S5 0716+714, the Swift-XRT operated in photon counting (PC) and windowed timing (WT) readout modes with a total exposure time of ~1.55×10^5 s. The data were processed using the XRTDAS software package (v3.7.0) with the release of CALDB (version 20220803). The cleaned events were produced using the `xrtpipeline` task, selecting events with grades 0–12 for PC mode and grades 0–2 for WT mode. For the PC mode, the source region was extracted from a circular region of 20 pixels (~47″) centered on the source. If the count rate was above 0.5 count s^{-1}, pileup correction was applied by excluding the central region events within 3″–10″, using an annulus with an outer radius of 20 pixels. The background region was extracted from an annulus with an inner radius of 80″ and an outer radius of 160″ centered on the source. For the WT mode, the source and background regions were extracted from circular regions of 20−30 pixels, depending on source

[9] https://swift.gsfc.nasa.gov/analysis/uvot_digest/sss_check.html

brightness and exposure time, with the source region centered on the source and the background region nearby. The high-level product data, including the spectra and ancillary response files, were generated from the cleaned data using the xrtproducts task. The spectra were grouped using the grppha (v3.1.0) tool to ensure at least one count per bin for fitting with Cash statistic (W. Cash 1979). The grouped spectra were loaded into XSPEC (v12.13.0c) and fitted with an absorbed power-law model with normalization energy $E_0 = 1$ keV. The Galactic hydrogen column density was fixed at $n_H = 2.88 \times 10^{20}\,\mathrm{cm}^{-2}$ (HI4PI Collaboration et al. 2016). In XSPEC settings, the solar abundances used in the photoelectric absorption models were set as wilm (J. Wilms et al. 2000), and the photoionization absorption cross sections were set as vern (D. A. Verner et al. 1996). For X-ray data fitting, the parameter errors correspond to 90% confidence errors ($\Delta\chi^2 = 2.706$). Finally, the unabsorbed fluxes and photon spectral indices were obtained.

2.2. NuSTAR Observation

NuSTAR, launched in 2012, operates in the hard X-ray range (3−79 keV) and features two telescopes with multilayer coatings that focus reflected X-rays onto pixelated CdZnTe focal plane modules, FPMA and FPMB. The observation provides a spectral resolution of approximately 1 keV, and the half-power diameter of an image of a point source is ~1′. Additional information can be found in F. A. Harrison et al. (2013).

NuSTAR observed S5 0716+714 with its two focal plane modules on 2015 January 24 (MJD 57046), with an exposure time of ~18.5 ks. The raw data were processed with the NuSTAR Data Analysis Software (v2.1.2) package using the calibration from the release of CALDB (version 20230307). The cleaned event files were produced by the nupipeline task. The source region was extracted from a circular region of 45″ centered on the centroid of X-ray emission. The background was extracted from a position 5′ away from the centroid of the X-ray emission, using a circular region of 1.°5. The spectra were produced from the cleaned event files and grouped with at least one count per bin using the nuproducts task. We focused on the energy range of 3−60 keV where the source was detected. The XSPEC settings (including the Galactic hydrogen column density) were the same as those used in the Swift-XRT analysis.

2.3. Fermi-LAT Observation

The Fermi Gamma-ray Space Telescope was launched in 2008, and it consists of two instruments: Gamma-ray Burst Monitor and LAT. The Fermi-LAT (W. B. Atwood et al. 2009) is capable of detecting γ-ray in the energy range from 20 MeV to beyond 300 GeV. The point-source sensitivity of Fermi-LAT is $\sim 2 \times 10^{-13}\,\mathrm{erg\,cm^{-2}\,s^{-1}}$ for the north celestial pole after 10 yr operation (M. Ajello et al. 2021).

We used data events from the Fermi-LAT's Pass 8 database in the period from MJD 57010 (2014 December 19) to 57075 (2015 February 22). The data were collected within an energy range of 0.1−100 GeV and within a 15° radius region of interest (ROI) centered on S5 0716+714. A maximum zenith angle value of 90° was selected to avoid background γ-rays from the Earth's limb. We performed an unbinned likelihood analysis of the data using the latest Fermitools (v2.2.0; Fermi Science Support Development Team 2019) and the instrument response functions P8R3_SOURCE_V3. The conditions "evclass=128, evtype=3" were used to filter events with a high probability of being photons, and "(DATA_QUAL $\geqslant$ 0) &&(LAT_CONFIG==1)" was used to select the good time intervals. The model file, generated by make4FGLxml Python package, included all the sources from the Fermi-LAT Fourth Source (S. Abdollahi et al. 2022) catalog within 25° of S5 0716 +714 as well as the Galactic (gll_iem_v07.fits) and extra-galactic isotropic (iso_P8R3_SOURCE_V3_v1.txt) diffuse emission components. The spectral parameters of sources with an average significance larger than 5σ within 5° of the ROI were left free, as well as sources within 10° of the ROI with a variable index $\geqslant$24.725 (S. Abdollahi et al. 2022). The best model between a power-law $\left[\mathrm{PL};\ \frac{dN}{dE} = N_0\left(\frac{E}{E_0}\right)^{-\Gamma_\gamma}\right]$ model and a log-parabola $\left[\mathrm{LP};\ \frac{dN}{dE} = N_0\left(\frac{E}{E_0}\right)^{-\left(\alpha+\beta\log\left(\frac{E}{E_0}\right)\right)}\right]$[10] model was selected by calculating the test statistic (TS) for curve spectrum $\mathrm{TS_{curve}} = 2(\log\mathcal{L}_{\mathrm{LP}} - \log\mathcal{L}_{\mathrm{PL}})$, where $\mathcal{L}_{\mathrm{PL}}/\mathcal{L}_{\mathrm{LP}}$ represent the maximum likelihood value of power law and log-parabola, respectively (P. L. Nolan et al. 2012; S. Abdollahi et al. 2022). If $\mathrm{TS_{curve}} \geqslant 16$, corresponding to 4σ, the model was switched to the log-parabola (LP) model. We found that S5 0716+714 preferred the power-law (PL) model rather than the LP model. We generated the light curves binned in the 1 day bin. In each time bin, the normalization parameters of the sources within 5° of ROI and the spectral index of the S5 0716+714 were allowed to vary freely during the spectral fitting. The rest of the parameters and other source models were frozen. The normalization of the two diffuse emission components was also set free in the analysis. We only included flux data points that are significantly detected with test statistic TS $\geqslant$ 16. Meanwhile, we calculated the 95% confidence level upper limit flux value for the case of TS < 16 using the UpperLimits[11] tool. While examining the SED, we fixed the spectral indices as the constant value equal to the value fitting over the whole energy range.

2.4. MAGIC Observation

We compiled the VHE γ-ray data, including the light curve and spectra, from MAGIC Collaboration et al. (2018), who divided the observation into two periods: Phase A (MJD 57040 −57050) and Phase B (MJD 57065−57070). The spectra have been corrected by the extragalactic background light (EBL) absorption using the redshift $z = 0.2304$ (A. Pichel et al. 2023) and the EBL model from A. Domìnguez et al. (2011).

After completing the data reduction, we present the multi-wavelength light curve, as shown in Figure 1.

3. Result and Discussion

3.1. The γ-Ray Variability Timescale

For the purpose of studying the geometry of the emission region and the property of the particle population, we modeled the light curve to explore the time profile and variability timescale. In this work, we used the Fermi γ-ray data to pursue

[10] Here, the "log" refers to the decimal logarithm, whereas "ln" in Equation (2) below denotes the natural logarithm.

[11] https://fermi.gsfc.nasa.gov/ssc/data/analysis/scitools/upper_limits.html

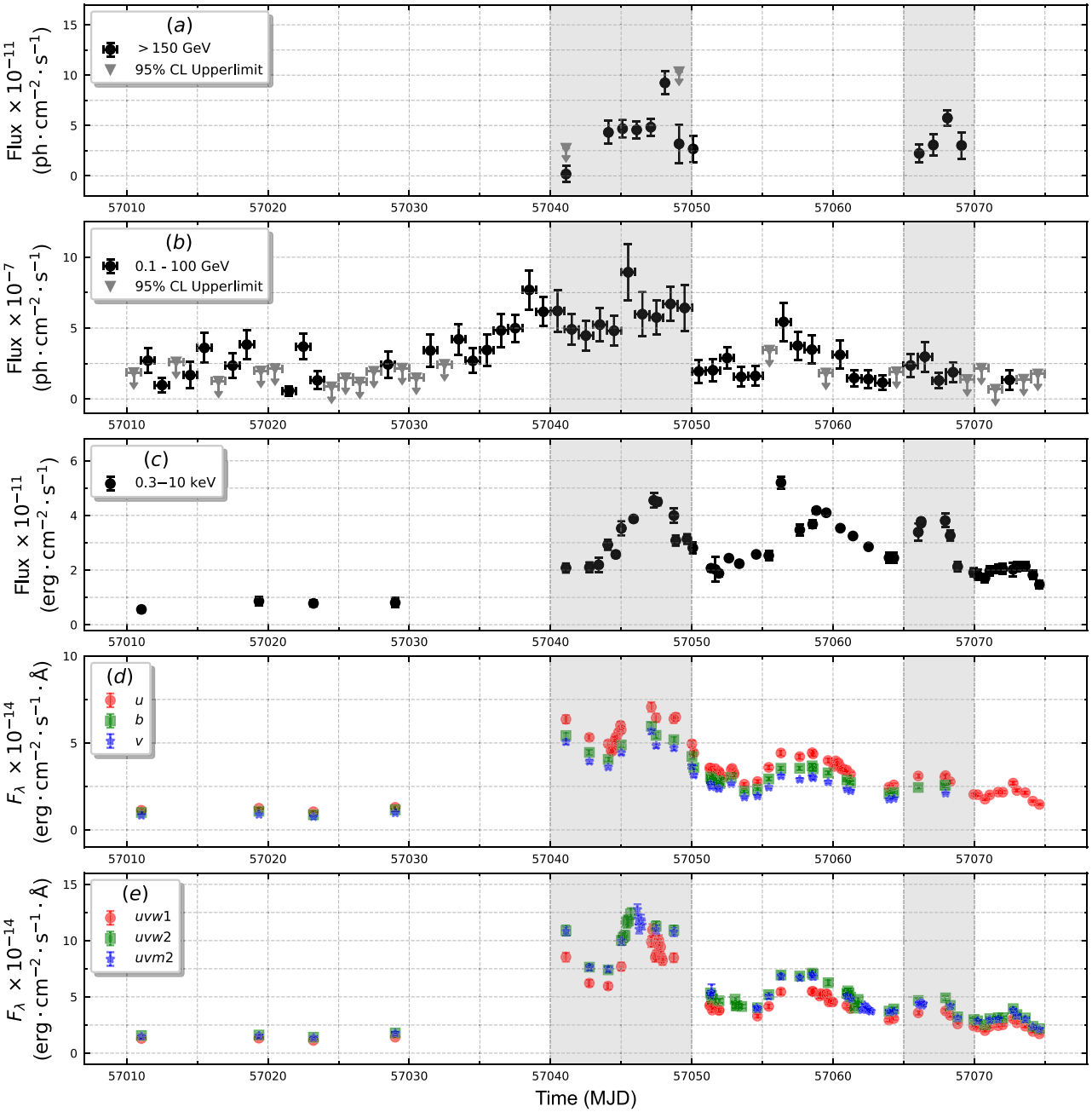

Figure 1. The multiwavelength light curve during the period from MJD 57010 to 57075 with Swift, Fermi, and MAGIC observations. From the top to bottom panels: (a) MAGIC VHE flux, >150 GeV, and the gray triangle is the 95% confidence level upper limit; (b) Fermi-LAT flux in 0.1−100 GeV in 1 day bin; (c) Swift-XRT flux, 0.3−10 keV; (d) Swift-UVOT, *u*, *b*, and *v* bands with the Galactic extinction correction; (e) Swift-UVOT, *uvw*1, *uvm*2, and *uvw*2 bands with the Galactic extinction correction. The two gray time intervals are the periods MAGIC observation was taken, meaning Phase A and Phase B.

this task as it is more continuously and uniformly sampled compared to the data of optical, UV, X-ray, and VHE bands. The exponential fitting is applied to each component of the flare; the entire light curve is, thus, expressed as a sum of exponential functions with a smoothed transition from raising to falling edge

$$F(t) = F_{\rm c} + \sum_i 2F_{0,i}\left[\exp\left(\frac{t_{0,i}-t}{T_{{\rm r},i}}\right) + \exp\left(\frac{t-t_{0,i}}{T_{{\rm d},i}}\right)\right]^{-1}, \quad (1)$$

where $F_{\rm c}$ is the baseline or constant flux, F_0 is the peak flux value at time t_0, and $T_{\rm r}$ and $T_{\rm d}$ are the rise and decay time, respectively (A. A. Abdo et al. 2010). We constructed a likelihood function for fitting the exponential functions and considered the contribution of the upper limit value to the likelihood function. The `iminuit` package was employed to perform the maximum likelihood fitting, and the Bayesian Information Criterion (BIC) was utilized to ascertain the optimal number of exponential functions required to fit the light curve:

$$\mathrm{BIC} = k\ln(N) - 2\ln(\hat{\mathcal{L}}), \quad (2)$$

where k is the number of model parameters, N is the total number of data points, and $\hat{\mathcal{L}}$ represents the maximized value

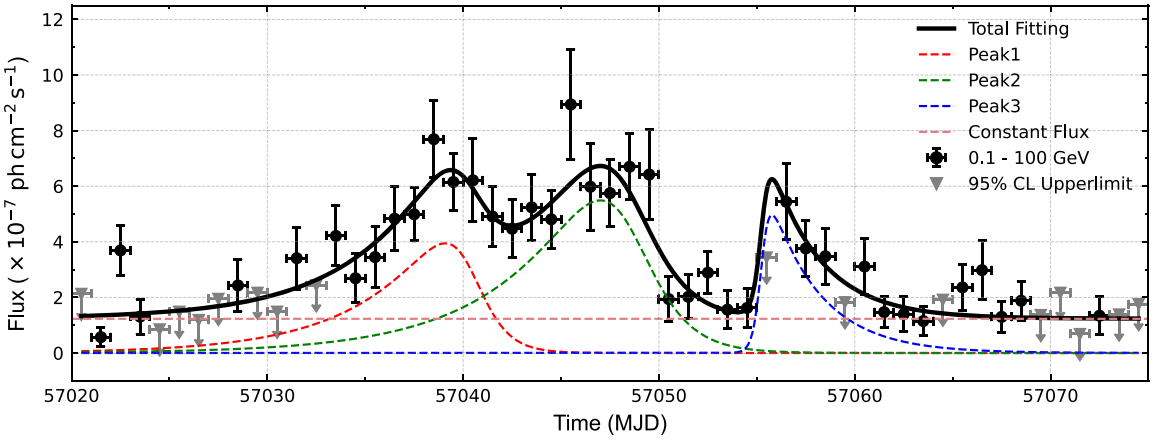

Figure 2. The fitted light curve of the period MJD 57020−57075. The dash lines with different colors represent the different peak components, and the solid black line represents the sum-fitted time profile of each component.

Table 1
Fitting Parameters of Light Curve in Figure 2

Component	t_0 (MJD)	F_0 (× 10^{-7} ph cm^{-2} s^{-1})	T_r (days)	T_d (days)
(1)	(2)	(3)	(4)	(5)
1	57040.27 ± 0.98	3.16 ± 1.38	4.34 ± 2.17	0.95 ± 0.76
2	57048.33 ± 1.99	4.75 ± 1.76	4.75 ± 3.89	1.48 ± 1.02
3	57055.26 ± 1.58	3.29 ± 2.39	0.23 ± 0.51	2.60 ± 1.23

Note. The constant flux is given as $F_c = (1.23 \pm 0.28) \times 10^{-7}$ ph cm^{-2} s^{-1}.

of the likelihood function for fitting the exponential functions (R. A. Edelson & J. H. Krolik 1988; E. Wit et al. 2012). We tested different numbers of exponential functions and selected the model that minimized the BIC value. Finally, we used three exponential components to fit the light curve from MJD 57020 to 57075, as shown in Figure 2, and the fitting parameters are listed in Table 1. It is important to note that a shorter time bin light curve can reveal more detailed structures and accurate variability timescales, but this comes with increased flux errors and reduced TS values, which can decrease the fitting quality.

Three peak profiles exhibited asymmetric shapes, reflecting the underlying particle acceleration and cooling mechanisms. The first two peaks showed a relatively gradual rise followed by a sharp decay, suggesting either a gradual acceleration of particles or rapid cooling or escape of injected/accelerated electrons, resulting in a radiative cooling timescale shorter than the acceleration timescale (N. Roy et al. 2019). In contrast, the third minor peak, which was also observed in other bands (see Figure 1) but lacked coverage in the VHE band, exhibited a relatively shorter rise timescale compared to its decay timescale, indicating that the asymmetry may stem from changes in the bulk Lorentz factor, the structure of the emission region's shells (N. Roy et al. 2019), or particle injection processes (G. Wang et al. 2022). Our findings on asymmetry differ from those of X. Geng et al. (2020), who reported symmetric flare profiles. This discrepancy arises because their analysis used shorter binning to construct the light curve, increasing the associated errors and leading to divergent results.

In addition, the rise and decay timescales can serve as a tool for constraining the geometry of the emission region, which will be explored in the following subsection.

3.2. Modeling Spectral Energy Distributions

The emission mechanisms of blazars can be better understood by modeling their SEDs. In this context, to further investigate the physical origin of the flaring activity of S5 0716 +714, we modeled the simultaneous multiwavelength SEDs during two distinct periods: Phase A (MJD 57040−57050) and Phase B (MJD 57065−57070). Despite the data we mentioned above, we collected simultaneously observed radio spectral data from MAGIC Collaboration et al. (2018), and the X-ray spectra were corrected through a deabsorption process employing the cross section in R. Morrison & D. McCammon (1983) and the hydrogen column density value (HI4PI Collaboration et al. 2016). Historical archival data were also obtained from the Space Science Data Center.[12]

Specifically, A. Wierzcholska & H. Siejkowski (2016) performed a cross correlation analysis between the optical, UV, and γ-ray bands during 2015 January and February. Their findings indicated no evident time lags among the optical, UV, and γ-ray emissions, suggesting they likely originate from the same region. The Swift-XRT X-ray band is also expected to exhibit zero time lag with the γ-ray band; however, the mismatched sampling in the Swift-XRT X-ray data could introduce artifacts affecting the correlation results (A. Wierzcholska & H. Siejkowski 2016). Therefore, the one-zone model shall be considered during the SED modeling. The popular method for estimating the (intrinsic) size of the emission region (R_b) assumes that the flux variability timescale corresponds to the light travel time across the emission region. In this context, the observed shortest doubling/halving timescale (t_{var}) can be used to constrain the size of the emission region, which is expressed as $R_b \leqslant \frac{ct_{var}\delta}{1+z}$ where δ is the Doppler factor. In our

[12] https://www.ssdc.asi.it/

estimations, $t_{\rm var}$ was calculated as $t_{\rm var} = \ln(2) \times \min\{T_{\rm r}, T_{\rm d}\}$ (see, e.g., B. Rani et al. 2013b; S. Gasparyan et al. 2018, using the rising and decay components in Phase A for SED modeling). Following U. Bach et al. (2005), we adopted $\delta = 30$, leading to an estimated emission region size of $R_{\rm b} \simeq 4 \times 10^{16}$ cm during our SED modeling. In the following, we performed the SED modeling using the public code jets SED modeler and fitting tool (JetSet; A. Tramacere et al. 2009, 2011; A. Tramacere 2020), and we considered two scenarios: (i) the broadband emission originated from the leptonic model, namely, synchrotron and IC radiation; and (ii) the emission originated from the lepto-hadronic hybrid model.

3.2.1. Leptonic Scenario

The one-zone leptonic scenario assumes that the emissions originate from a spherical region (blob) of the radius $R_{\rm b}$, filled with a uniform magnetic field (B). This region, located within the blazar jet, moves with a bulk Lorentz factor ($\Gamma = \frac{1}{\sqrt{1-\beta_\Gamma^2}} \sim \delta$, where $\beta_\Gamma c$ is the speed of the blob) at a small viewing angle to the observer, resulting in Doppler-boosted emission characterized by a Doppler factor (δ). Blazar emission is primarily dominated by radiation from synchrotron and IC processes. When the low-energy seed photons for the IC process originate from synchrotron radiation, the process is referred to as SSC (e.g., J. D. Finke et al. 2008). Alternatively, if the seed photons come from external regions such as the accretion disk (AD; C. D. Dermer & R. Schlickeiser 1993), the broad-line region (BLR; M. Sikora et al. 1994), or the dust torus (DT; M. Błażejowski et al. 2000), the process is termed EC process.

The blob is assumed to be filled with relativistic electrons with a log-parabola with low-energy power-law branch distribution, expressed as follows:

$$N_e(\gamma) = A_e n_e(\gamma) = A_e \begin{cases} \left(\frac{\gamma}{\gamma_{e,0}}\right)^{-s}, & \gamma_{e,\min} < \gamma < \gamma_{e,0} \\ \left(\frac{\gamma}{\gamma_{e,0}}\right)^{-\left(s + r\log\left(\frac{\gamma}{\gamma_{e,0}}\right)\right)}, & \gamma_{e,0} < \gamma < \gamma_{e,\max} \end{cases}. \quad (3)$$

Here, A_e is defined by the actual density of relativistic electrons (N_e) in units of per cubic centimeter with $A_e = \frac{N_e}{\int n_e(\gamma) d\gamma}$ (see the documentation in JetSet), s is the spectral index, r is the spectral curvature, and $\gamma_{e,\,\min/0/\max}$ are the minimum, turnover, and maximum electron Lorentz factor, respectively.

S5 0716+714 is a BL Lac object, allowing us to model the SEDs using the one-zone SSC model. The SSC model is described by nine parameters, where six of these parameters characterize the electron energy distribution ($\gamma_{e,\,\min/0/\max}$, N_e, s, and r), while the remaining three describe the properties of the emission region ($R_{\rm b}$, B, and δ). During the SSC modeling, the size of the emission region, $R_{\rm b}$, was fixed at 4×10^{16} as mentioned above, and the minimum and maximum electron Lorentz factors were fixed at 1 and 10^7, respectively. The other parameters were optimized to achieve the best-fit model. The best-fitted model parameters are summarized in Table 2, and the resulting best-fit SSC model SEDs are presented in Figure 3.

However, the SSC model failed to reproduce the large separation between the low-energy peak (~10^{14}–10^{15} Hz) and the high-energy peak (~10^{24}–10^{25} Hz) using a Doppler factor of $\delta = 30$ (U. Bach et al. 2005). Such a large separation required an extreme Doppler factor ($\delta \sim 200$, see Table 2); otherwise, the observed optical flux would be underestimated. Moreover, a hard electron spectral index and a low magnetic field were also required. These difficulties could be avoided by assuming that the high-energy (HE)/VHE γ-ray emissions originate from a more highly boosted substructure within the jet. For example, the "jets-in-a-jet" model could have an extra Lorentz factor due to the plasma material outflowing from the reconnection regions (D. Giannios et al. 2009). However, this scenario typically results in fast variability, as observed in sources like Mrk 501, PKS 2155-304, 3C 279, and M87 (J. Albert et al. 2007; F. Aharonian et al. 2007; D. Giannios et al. 2010; A. Shukla & K. Mannheim 2020), which contradicts the variability observed in S5 0716+714.

One can calculate the jet power and further understand the composition of the jet. The jet power ($P_{\rm jet}$) carried by relativistic electrons (P_e), cold protons ($P_{p,\,\rm cold}$), and magnetic field (P_B) is estimated via

$$P_{\rm jet} = \sum_i \pi R_{\rm b}^2 \Gamma^2 \beta_\Gamma c U_i, \quad (4)$$

where the U_i is the energy density of the relativistic electrons (U_e), cold protons ($U_{p,\,\rm cold}$), and magnetic field (U_B), respectively, in the comoving frame (G. Ghisellini et al. 2010). These energy densities can be derived by

$$U_B = \frac{B^2}{8\pi}, \quad (5)$$

$$U_e = m_e c^2 \int \gamma N_{\rm e}(\gamma) d\gamma, \quad (6)$$

$$U_{p,\,\rm cold} = m_p c^2 1 \int N_e(\gamma) d\gamma, \quad (7)$$

where, assuming a cold-proton-to-electron number density ratio of 1, B is the magnetic field strength obtained from the SED modeling, and m_e and m_p are the rest mass of the electron and proton, respectively. The jet powers and the energy densities are calculated and listed in Table 2. The Eddington luminosity of the supermassive black hole (SMBH) is

$$L_{\rm Edd} = 2\pi m_p c^3 R_{\rm S}/\sigma_{\rm T}, \quad (8)$$

where $\sigma_{\rm T}$ is the Thompson scattering cross section, $R_{\rm S} = 2GM_{\rm BH}/c^2$ is the Schwarzschild radius of the SMBH, and $M_{\rm BH}$ is the mass of SMBH. Using the $M_{\rm BH} = 10^{8.91} M_\odot$ for S5 0716+714 (H. T. Liu et al. 2019) where $M_\odot$ is the mass of the Sun, the Eddington luminosity of the source is calculated as $L_{\rm Edd} = 1.02 \times 10^{47}\,{\rm erg\,s^{-1}}$. It is worth noting that the jet powers in two phases under the SSC model moderately exceed the Eddington luminosity, primarily due to the extreme Doppler factors required to account for the SSC model.

As discussed above, the HE/VHE γ-ray emissions probably require a substructure within the jet to account for the large separation between the two peaks of the SEDs. Alternatively, these emissions could arise from an additional radiation component, such as the EC or hadronic component, which

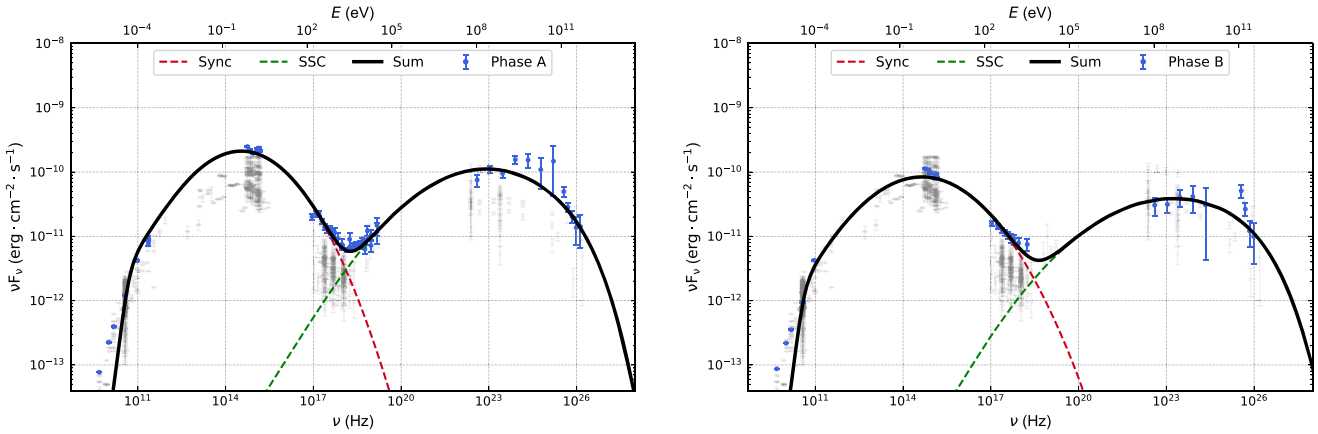

Figure 3. One-zone SSC modeling. The left panel is for Phase A (MJD 57040–57050); the right one is for Phase B (MJD 57065–57070). The VHE spectra are corrected by EBL absorption adopting $z = 0.2304$. The meanings of line styles are given in the legend.

Table 2
Parameters for the Broadband SEDs for Different Models

Params	Units	Phase A			Phase B		
		SSC	SSC+EC	SSC+*pp* Interactions	SSC	SSC+EC	SSC+*pp* Interactions
(1)	(2)	(3)	(4)	(5)	(6)	(7)	(8)
$R_{\rm b}^{\dagger}$	cm	4.00×10^{16}	4.00×10^{16}	4.00×10^{16}	4.00×10^{16}	4.00×10^{16}	4.00×10^{16}
B	G	4.45×10^{-3}	8.35×10^{-2}	1.95×10^{-1}	3.78×10^{-3}	7.10×10^{-2}	1.61×10^{-1}
δ		204.44	73.95	30 †	188.40	57.84	30†
$\gamma_{e,\,\rm min}$		1 †	77.44	1†	1†	96.69	1†
$\gamma_{e,\,\rm max}$ †		10^7	10^7	10^7	10^7	10^7	10^7
N_e	$\rm cm^{-3}$	123.81	25.37	2071.33	104.12	23.85	1674.66
$\gamma_{e,\,0}$		911.98	2540.8	1863.48	414.73	2961.56	329.75
s		1.57	2.54	1.99	1.52	2.55	1.85
r		0.64	0.78	0.87	0.47	0.59	0.48
$\tau_{\rm BLR}^{\dagger}$		...	0.1	...	...	0.1	...
$T_{\rm DT}^{\dagger}$	K	...	1200	...	...	1200	...
$\tau_{\rm DT}^{\dagger}$		...	0.1	...	...	0.1	...
$L_{\rm Disk}^{\dagger}$	$\rm erg\ s^{-1}$	...	2×10^{42}	...	...	2×10^{42}	...
$T_{\rm Disk}^{\dagger}$	K	...	2×10^4	...	...	2×10^4	...
$\theta_{\rm open}^{\dagger}$	deg	...	5	...	...	5	...
$R_{\rm H}^{\dagger}$	cm	...	4.57×10^{17}	...	...	4.57×10^{17}	
$\gamma_{p,\,\rm min}$ †		...	...	1	...	...	1
$\gamma_{p,\,\rm max}$ †		...	...	1000	...	...	1000
N_p	$\rm cm^{-3}$	...	...	3185.17	...	...	1318.35
$\gamma_{p,\,\rm cut}^{\dagger}$		...	...	100	...	...	100
α_p		...	...	2.25	...	...	2.07
$n_{\rm H}^{\dagger}$	$\rm cm^{-3}$	...	...	10^4	...	...	10^4
f_{pp}		...	...	1.20×10^{-5}	...	...	1.20×10^{-5}
U_e	$\rm erg\ cm^{-3}$	5.60×10^{-3}	4.26×10^{-3}	1.60×10^{-2}	4.79×10^{-3}	4.97×10^{-3}	1.72×10^{-2}
$U_{p,\,\rm cold}$	$\rm erg\ cm^{-3}$	1.86×10^{-1}	3.81×10^{-2}	1.50×10^{1}	1.57×10^{-1}	3.59×10^{-2}	1.50×10^{1}
U_B	$\rm erg\ cm^{-3}$	7.89×10^{-7}	2.77×10^{-4}	1.51×10^{-3}	5.68×10^{-7}	2.01×10^{-4}	1.03×10^{-3}
P_e	$\rm erg\ s^{-1}$	3.53×10^{46}	3.51×10^{45}	2.16×10^{45}	2.56×10^{46}	2.51×10^{45}	2.33×10^{45}
P_B	$\rm erg\ s^{-1}$	4.97×10^{42}	2.28×10^{44}	2.05×10^{44}	3.04×10^{42}	1.01×10^{44}	1.39×10^{44}
$P_{p,\,\rm cold}$	$\rm erg\ s^{-1}$	1.17×10^{48}	3.14×10^{46}	2.04×10^{48}	8.37×10^{47}	1.81×10^{46}	2.04×10^{48}
$U_{\rm BLR}$	$\rm erg\ cm^{-3}$	...	2.70×10^{-10}	...	...	2.93×10^{-10}	...
$U_{\rm DT}$	$\rm erg\ cm^{-3}$	...	1.84×10^{-4}	...	...	1.13×10^{-4}	...
$U_{p,\,\rm rel}$	$\rm erg\ cm^{-3}$	...	...	1.52×10^{1}	...	...	7.70×10^{0}
$P_{p,\,\rm rel}$	$\rm erg\ s^{-1}$	...	...	2.07×10^{48}	...	...	1.04×10^{48}
$P_{\rm tot}$	$\rm erg\ s^{-1}$	1.21×10^{48}	3.52×10^{46}	4.11×10^{48}	8.63×10^{47}	2.07×10^{46}	3.09×10^{48}

Note. Parameters with the symbol "†" represent that they keep frozen in the SED fitting. The redshift is adopted as 0.2304. The symbol "..." represents a null value. The Eddington luminosity is calculated as $L_{\rm Edd} = 1.02 \times 10^{47}$ erg s^{-1} for the SMBH mass $10^{8.91} M_{\odot}$ for S5 0716+714 (H. T. Liu et al. 2019).

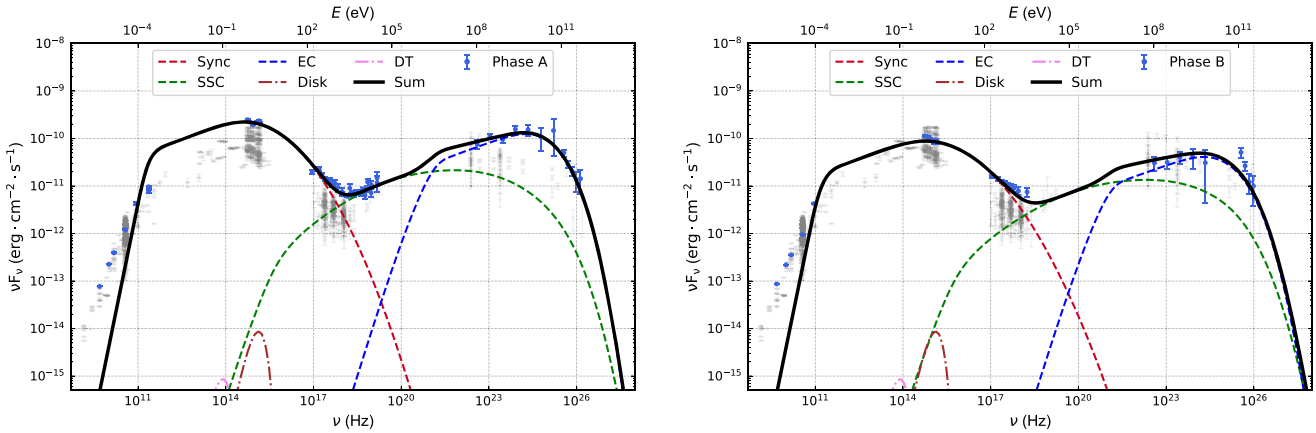

Figure 4. One-zone SSC plus EC modeling. The left panel is for Phase A (MJD 57040−57050); the right one is for Phase B (MJD 57065−57070). The VHE spectra are corrected by EBL absorption adopting $z = 0.2304$. The meanings of line styles are given in the legend, where the EC line includes the contribution from EC-BLR and EC-DT.

will be explored in the upcoming content and the next subsection, respectively.

Previous studies have conducted SED modeling for S5 0716+714; however, they also found that the SSC model failed to reproduce the SEDs (e.g., G. Tagliaferri et al. 2003; B. Rani et al. 2013a; N. H. Liao et al. 2014). In MAGIC Collaboration et al. (2018), they attempted the one-zone SSC model but found it underestimated the observed optical flux. Therefore, the EC component is a plausible mechanism for accounting for the HE/VHE γ-ray emissions, assuming the scattering of weak external emissions, despite the absence of detected thermal components or emission lines (M. S. Shaw et al. 2009; N. H. Liao et al. 2014). Following this, we explored the SSC model combined with an EC component. Assuming a conical jet with a half-opening angle of $\theta_{\rm open} = 5^{\circ}$, the distance of the emission region from the central engine ($R_{\rm H}$) was calculated to be ~0.15 pc. We considered BLR as a spherical shell with an inner and outer radius of $R_{\rm BLR,in} = 3 \times 10^{17}(L_{\rm disk}/10^{46})^{1/2}$ cm and $1.1 \times R_{\rm BLR,in}$ (S. Kaspi et al. 2007) with a coverage factor of $\tau_{\rm BLR} = 0.1$, where $L_{\rm disk}$ is the AD luminosity. The DT was assumed to be a radius of $R_{\rm DT} = 2 \times 10^{19}(L_{\rm disk}/10^{46})^{1/2}$ cm (K. Cleary et al. 2007) with a reprocessing factor $\tau_{\rm DT} = 0.1$. The DT and AD temperatures were fixed at 1.2×10^3 K and 2×10^4 K, respectively. The actual disk luminosity ($L_{\rm disk}$) is challenging to constrain due to the featureless optical spectra of S5 0716+714. Therefore, we fixed a reasonable disk luminosity value of 2×10^{42} erg s^{-1} during the SED modeling in two phases. This value was estimated according to the SED modeling and is below the upper limits reported in G. Ghisellini et al. (2010) and C. W. Danforth et al. (2013), making it a reasonable choice. Furthermore, the minimum electron Lorentz factor, $\gamma_{\rm e,min}$, was also left as a free parameter. The best-fit models are displayed in Figure 4, with the corresponding parameters listed in Table 2.

We can see that the SSC plus EC model provides a good fit to the SEDs and successfully reproduces the γ-ray emissions. This is consistent with earlier studies, where the inclusion of EC components also successfully accounted for the SEDs (G. Tagliaferri et al. 2003; B. Rani et al. 2013a; N. H. Liao et al. 2014). The jet powers derived from this model using Equation (4) are listed in Table 2 and remain below the Eddington luminosity in both phases. This model requires a high Doppler factor of $\delta = 73.95$ for Phase A and $\delta = 57.84$ for Phase B, which are not preferred in such models for the causality of light traveling across the emission region. While a higher Doppler factor corresponds to a larger variability timescale in the blob frame, such a variability timescale could not be associated with the light-crossing but with the particle cooling processes or changes in external radiation fields. Moreover, such high Doppler factors derived from the SED modeling remain problematic due to the maximum apparent velocity of $\beta_{\rm app}^{\rm max} \sim 34.4$ estimated from M. L. Lister et al. (2018). Consequently, this model is excluded from our consideration.

3.2.2. Lepto-hadronic Hybrid Scenario

As mentioned above, the hadronic radiation component could be the origination to produce the γ-ray emissions. The proton–proton (pp) interactions have been used to explain the SEDs of blazars (e.g., P. Banik & A. Bhadra 2019; P. Banik et al. 2020). In the work of W.-J. Li et al. (2022), they suggested that pp interactions could be important for blazars and have a parameter space to interpret the γ-ray spectra. Meanwhile, R. Xue et al. (2022) showed that pp interactions can explain the TeV spectra. Therefore, we incorporated the pp interactions into the one-zone SSC model to reproduce the SEDs following the parameters developed by S. R. Kelner et al. (2006). The pp interactions will produce secondary neutral (π^0) and charged ($\pi^{\pm}$) pions, which will decay into electrons/positrons ($e^{\pm}$), neutrinos (ν), and γ-ray emissions. The pp interactions are comprised of the following:

$$p + p \longrightarrow \begin{cases} p \\ \pi^0 \longrightarrow \gamma + \gamma \\ \pi^+ \longrightarrow \mu^+ + \nu_\mu \longrightarrow e^+ + \nu_e + \bar{\nu}_\mu + \nu_\mu \\ \pi^- \longrightarrow \mu^- + \bar{\nu}_\mu \longrightarrow e^- + \bar{\nu}_e + \nu_\mu + \bar{\nu}_\mu \end{cases}. \quad (9)$$

We adopted the analytical results from W.-J. Li et al. (2022), which indicate that, if the γ-ray emissions originate from π^0 decay and the jet power does not exceed the Eddington luminosity, the size of the emission region is constrained by

$$\frac{R_{\rm b}}{R_{\rm S}} \leqslant \frac{\sigma_{pp}}{12\sigma_{\rm T}} \frac{L_{\rm Edd}}{L_{\rm TeV}^{\rm obs}}, \quad (10)$$

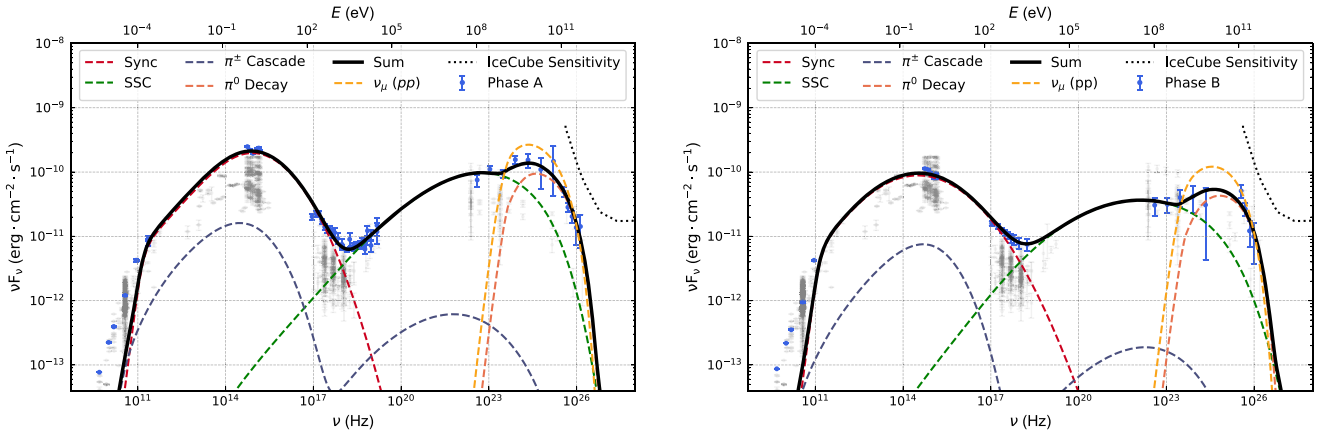

Figure 5. One-zone SSC plus *pp* modeling. The left panel is for Phase A (MJD 57040−57050); the right one is for Phase B (MJD 57065−57070). The VHE spectra are corrected by EBL absorption adopting $z = 0.2304$. The meanings of line styles are given in the legend. The dashed yellow line is the expected muon neutrino flux produced by the $\pi^{\pm}$ cascade through *pp* interactions. The dotted black line represents the IceCube sensitivity for decl. $\delta_{\rm del} = 60$ using the 10 yr data set from K. Ghiassi & J. Salwén (2023).

where $\sigma_{pp} \approx 6 \times 10^{-26}\,{\rm cm}^2$ is the cross section for *pp* interactions (S. R. Kelner et al. 2006), and $L_{\rm TeV}^{\rm ob}$ is the observed TeV luminosity. Applying the method from R. Xue et al. (2019) to calculate $L_{\rm TeV}^{\rm ob}$, we found that the maximum allowable $R_{\rm b}$ is constrained to $\sim 10^{13}$ cm. This implies a very compact emission region, smaller than the Schwarzschild radius ($R_{\rm S} = 2.44 \times 10^{14}$ cm) of S5 0716+714, which is atypical for blazars. Consequently, the jet power somewhat exceeding the Eddington luminosity appears necessary, which is plausible during a flaring state (P. Banik & A. Bhadra 2019; S. Gao et al. 2019; P. Banik et al. 2020). At the same time, Equation (11) in W.-J. Li et al. (2022), which estimates the number density of cold protons ($n_{\rm H}$), was deemed inapplicable here.

We assumed that the relativistic protons follow a power law with an exponential cutoff distribution:

$$N_p(\gamma) = A_p n_p(\gamma) = A_p \gamma^{-\alpha_p} \exp\left(-\frac{\gamma}{\gamma_{p,\,\rm cut}}\right),$$
$$\gamma_{p,\,\rm min} < \gamma < \gamma_{p,\,\rm max}. \quad (11)$$

Here, $A_p = N_p \frac{1}{\int n_p(\gamma) d\gamma}$, where N_p refers to the actual density of relativistic protons in units of per cubic centimeter. The parameter α_p is the power-law spectral index; $\gamma_{p,\,\rm min/cut/max}$ are the minimum, exponential cutoff, and maximum proton Lorentz factors, respectively. The efficiency of *pp* interactions (f_{pp}) depends on the density of cold protons and can be estimated using the expression

$$f_{pp} = K_{pp} \sigma_{pp} n_{\rm H} R_{\rm b}, \quad (12)$$

where $K_{pp} \approx 0.5$ is the inelasticity coefficient, and $n_{\rm H}$ is the number density of cold protons (S. R. Kelner et al. 2006). We set the number density of cold protons $n_{\rm H} = 10^4\,{\rm cm}^{-3}$ and the proton Lorentz factors $\gamma_{p,\,\rm min/cut/max} = 1/10^2/10^3$ in our modeling. The cold proton column density would be $N_{\rm H,cold} \simeq n_{\rm H} R_{\rm b} \simeq 4 \times 10^{20}\,{\rm cm}^{-2}$, making the optical/UV and X-ray emission absorbed via the photoionization absorption process. The optical depth for scattering is $\tau_{\rm sc} = \sigma_{\rm sc} n_{\rm H} R_{\rm b}$ where $\sigma_{\rm sc}$ is the scattering cross section, expressed by

$$\sigma_{\rm sc} = \sigma_{\rm T} \frac{3}{4}\left[\frac{1+x}{x^3}\left\{\frac{2x(1+x)}{1+2x} - \ln(1+2x)\right\} + \frac{1}{2x}\ln(1+2x) - \frac{1+3x}{(1+2x)^2}\right], \quad (13)$$

with $x = E/(m_e c^2)$, and E represents the photon energy (see R.-Y. Liu et al. 2019). The resulting flux should be multiplied by a factor of $(1 - \exp(-\tau_{\rm sc}))/\tau_{\rm sc}$. However, the absorption effect is negligible since $\tau_{\rm sc} \ll 1$ was obtained. During the modeling, the Doppler factor was fixed at 30; the minimum electron Lorentz factor was set to 1, while the remaining parameters were treated as free. The fitting results are presented in Figure 5 with the corresponding parameters listed in Table 2.

The results indicate that the γ-ray emissions generated by π^0 decay via *pp* interactions successfully reproduce the SEDs. Additionally, the synchrotron emission from secondary electron pairs contributes marginally to the radio and X-ray fluxes compared to the emission from primary electrons. The energy densities of the cold protons and relativistic protons in the SSC plus *pp* model are calculated as follows:

$$U_{p,\,\rm cold} = m_p c^2 n_{\rm H}, \quad (14)$$

$$U_{p,\,\rm rel} = m_p c^2 \int \gamma N_p(\gamma) d\gamma. \quad (15)$$

The total jet power is estimated to be $P_{\rm jet} = 4.11 \times 10^{48}\,{\rm erg\,s^{-1}}$ for Phase A and $P_{\rm jet} = 3.09 \times ;10^{48}\,{\rm erg\,s^{-1}}$ for Phase B, which exceed the Eddington luminosity by a factor of 30–40, as detailed in Table 2. An enhanced activity may result in a transient increase in jet power, potentially exceeding the Eddington luminosity, as discussed above. Alternatively, in the case of a highly collimated jet outflow, the Eddington luminosity can be exceeded because the jet does not interfere with the accretion flow (S. Gao et al. 2019). Moreover, VLBI analysis by MAGIC Collaboration et al. (2018) suggests that a superluminal knot passing through a recollimation shock may occur during this flaring state. Such interactions may increase the number density of electrons and protons in the emission region, further driving the jet power to exceed the Eddington luminosity.

The dashed yellow line in Figure 5 shows the muon neutrino (ν_μ) flux produced by $\pi^{\pm}$ cascade. It is necessary to evaluate the possible neutrino emission under the hadronic model. The corresponding neutrino event rate can be estimated via

$$\frac{dN_{\nu_\mu}}{dt} = \int_{E_{\nu_\mu,\,\mathrm{min}}}^{E_{\nu_\mu,\,\mathrm{max}}} dE_{\nu_\mu} A_{\mathrm{eff}}(E_{\nu_\mu}, \delta_{\mathrm{del}}) \phi_{E_{\nu_\mu}}, \tag{16}$$

where $E_{\nu_\mu,\,\mathrm{min}}$ and $E_{\nu_\mu,\,\mathrm{max}}$ are the lower and upper limits of the neutrino energy, respectively, $A_{\mathrm{eff}}(E_{\nu_\mu}, \delta_{\mathrm{del}})$ is the effective area in given decl. (δ_{del}), and $\phi_{E_{\nu_\mu}}$ is the muon neutrino differential energy flux. Then, the expected neutrino event rates for S5 0716+714, using the effective area from T. Carver (2019), are 0.69 events yr^{-1} for Phase A and 0.52 events yr^{-1} for Phase B, respectively. However, the IceCube did not detect any neutrino events from S5 0716+715, because the expected neutrino flux was below its cumulative sensitivity, making it insufficient to detect such events from this source, as shown in the dotted black line in Figure 5.

In addition to the models mentioned above, the two-zone SSC model was also explored in MAGIC Collaboration et al. (2018), which considers the interaction between a superluminal knot and a recollimation shock within the jet. While this two-zone model provides a better fit to the SED, it cannot fully reproduce the observations in the 10–100 GeV range. Furthermore, other jet models, such as the structured jet model (MAGIC Collaboration et al. 2018) and the helical magnetic field model (S. Chandra et al. 2015), have also been investigated during this flaring period. These various models indicate the complexity of the emission mechanisms during flaring states, suggesting that further multiwavelength observations are needed to fully capture the underlying processes.

4. Summary

In this study, we conducted a multiwavelength analysis of the 2015 flare of S5 0716+714 to investigate its radiation mechanisms. The data were gathered from the Swift-UVOT, Swift-XRT, NuSTAR, and Fermi-LAT databases, along with the MAGIC VHE data from the literature. These observations allowed us to estimate the size of the emission region, while the modeling of the broadband SEDs for Phase A and Phase B provided valuable insights into the physical processes occurring during the flaring periods. The main results are as follows. The size of the γ-ray emission region was estimated using the variability timescale, determined through exponential function fitting. Subsequently, one-zone models, including leptonic and lepto-hadronic hybrid scenarios, were employed to reproduce the SEDs for Phase A and Phase B. However, the SSC models could not adequately describe the SEDs without invoking extreme Doppler factors, potentially requiring an additional Lorentz factor as suggested in the "jets-in-a-jet" model. The SSC plus EC model provided a good fit to the SEDs but required a high Doppler factor, leading to its exclusion from our consideration. Additionally, the SSC plus *pp* interactions model was explored, and the results demonstrated that this model successfully reproduced the SEDs. Nevertheless, the total jet power in this scenario exceeded the Eddington luminosity, a situation that is still plausible due to the flaring state or the presence of a highly collimated jet.

Acknowledgments

H.B.X. acknowledges the support from the Shanghai Science and Technology Fund (22YF1431500), the National Natural Science Foundation of China (NSFC 12203034), and the science research grants from the China Manned Space Project. M.M. acknowledges the Croatian Science Foundation (HrZZ) Project IP-2022-10-4595. R.X acknowledges the support from the NSFC under grant No. 12203043. G.W. acknowledges the support from the China Postdoctoral Science Foundation (grant No. 2023M730523). S.H.Z. acknowledges support from the National Natural Science Foundation of China (grant No. 12173026), the National Key Research and Development Program of China (grant No. 2022YFC2807303), the Shanghai Science and Technology Fund (grant No. 23010503900), the Program for Professor of Special Appointment (Eastern Scholar) at Shanghai Institutions of Higher Learning, and the Shuguang Program (23SG39) of the Shanghai Education Development Foundation and Shanghai Municipal Education Commission. J.H.F. acknowledges the support from the NSFC 12433004, NSFC U2031201, the Scientific and Technological Cooperation Projects (2020–2023) between the People's Republic of China and the Republic of Bulgaria, the science research grants from the China Manned Space Project with No. CMS-CSST-2021-A06, and the support for Astrophysics Key Subjects of Guangdong Province and Guangzhou City. This research was partially supported by the Bulgarian National Science Fund of the Ministry of Education and Science under grants KP-06-H38/4 (2019), KP-06-KITAJ/2 (2020), and KP-06-H68/4 (2022).

Appendix
Swift Observation Data

The Swift-XRT best-fit parameters with an absorbed power-law model are shown in Table 3.

The Swift-UVOT aperture photometric data after the Galactic extinction correction are shown in Table 4.

Table 3
Swift-XRT Observations

ObsID (1)	Mode (2)	Exposure (3)	Time (4)	Γ_X (5)	$\Gamma_{X,err}$ (6)	N_0 (7)	$N_{0,\ err}$ (8)	Flux (9)	$Flux_{err}$ (10)	C-statistic (11)	d.o.f. (12)
00035009143	PC	921.50	57,011.04	2.18	0.23	1.08E-03	1.62E-04	5.60E-12	9.57E-13	72.59	91
00035009144	PC	1066.34	57,019.35	1.78	0.18	1.32E-03	1.71E-04	8.61E-12	1.63E-12	142.18	137
00035009145	PC	1051.36	57,023.21	2.26	0.18	1.55E-03	1.82E-04	7.80E-12	1.00E-12	99.42	138
00035009146	PC	829.10	57,029.01	1.81	0.22	1.27E-03	1.88E-04	8.08E-12	1.78E-12	119.58	105
00035009147	PC	991.42	57,041.09	2.22	0.12	4.08E-03	3.01E-04	2.08E-11	1.72E-12	187.33	217
00035009148	PC	1103.80	57,042.75	2.11	0.11	3.93E-03	2.92E-04	2.10E-11	1.87E-12	199.73	230
00035009149	PC	968.95	57,043.41	2.05	0.15	4.01E-03	3.91E-04	2.19E-11	2.65E-12	156.73	179
00035009152	PC	1356.03	57,044.02	2.29	0.09	5.85E-03	3.53E-04	2.93E-11	1.91E-12	224.78	259
00035009153	PC	6912.53	57,044.29	2.19	0.06	4.98E-03	1.90E-04	2.57E-11	1.12E-12	349.31	382
00035009154	PC	998.94	57,045.01	2.31	0.11	7.10E-03	4.85E-04	3.53E-11	2.57E-12	168.92	228
00035009156	PC	9574.62	57,045.14	2.43	0.04	7.95E-03	2.19E-04	3.87E-11	1.09E-12	425.84	425
00035009157	PC	1688.17	57,047.14	2.42	0.09	9.34E-03	5.32E-04	4.55E-11	2.65E-12	211.43	249
00035009158	PC	6557.90	57,047.22	2.46	0.05	9.28E-03	2.67E-04	4.50E-11	1.31E-12	352.41	391
00035009159	PC	1490.88	57,048.73	2.38	0.10	8.14E-03	5.15E-04	3.99E-11	2.62E-12	211.88	226
00035009160	PC	1490.88	57,048.86	2.41	0.10	6.32E-03	3.86E-04	3.08E-11	1.93E-12	189.58	238
00035009161	PC	1490.88	57,049.66	2.28	0.08	6.26E-03	3.31E-04	3.14E-11	1.79E-12	247.94	285
00035009162	WT	1007.11	57,050.01	2.73	0.12	5.77E-03	4.11E-04	2.81E-11	2.05E-12	222.56	247
00035009167	PC	3161.58	57,051.26	2.02	0.06	3.73E-03	1.65E-04	2.07E-11	1.15E-12	328.36	366
00035009164	WT	198.21	57,051.66	2.37	0.37	4.12E-03	8.68E-04	2.02E-11	4.47E-12	60.00	87
00035009168	PC	2469.83	57,051.85	2.09	0.07	3.50E-03	1.76E-04	1.88E-11	1.15E-12	291.47	329
00035009169	WT	5488.26	57,052.27	2.25	0.06	4.82E-03	1.58E-04	2.43E-11	8.90E-13	472.61	515
00035009170	WT	6144.92	57,052.99	2.21	0.06	4.36E-03	1.39E-04	2.23E-11	8.23E-13	548.34	553
00035009171	WT	5502.71	57,054.46	2.29	0.05	5.15E-03	1.47E-04	2.57E-11	8.00E-13	471.24	518
00035009172	WT	1082.94	57,055.45	2.37	0.11	5.15E-03	3.38E-04	2.53E-11	1.74E-12	242.50	266
00035009173	WT	1072.83	57,056.31	2.51	0.07	1.08E-02	4.64E-04	5.20E-11	2.25E-12	301.62	329
00035009174	PC	1483.39	57,057.64	2.34	0.08	7.01E-03	3.70E-04	3.47E-11	1.93E-12	262.78	269
00035009175	WT	2069.23	57,058.52	2.45	0.06	7.57E-03	2.84E-04	3.68E-11	1.40E-12	348.40	384
00035009176	WT	5406.15	57,058.65	2.46	0.04	8.62E-03	1.90E-04	4.18E-11	9.35E-13	494.67	549
00035009177	WT	13,689.18	57,059.05	2.49	0.02	8.46E-03	1.17E-04	4.10E-11	5.69E-13	739.93	696
00035009178	WT	12,428.53	57,060.05	2.47	0.03	7.29E-03	1.21E-04	3.53E-11	5.93E-13	636.68	682
00035009179	WT	12,276.77	57,061.04	2.41	0.03	6.65E-03	1.17E-04	3.25E-11	5.86E-13	602.31	683
00035009180	WT	16,028.34	57,062.05	2.42	0.03	5.85E-03	9.51E-05	2.85E-11	4.75E-13	605.02	701
00035009181	WT	1122.72	57,063.96	2.39	0.11	5.01E-03	3.52E-04	2.45E-11	1.78E-12	206.55	252
00035009182	WT	978.13	57,064.30	2.60	0.13	5.06E-03	3.92E-04	2.44E-11	1.89E-12	197.69	228
00035009184	WT	648.52	57,066.03	2.27	0.14	6.74E-03	5.79E-04	3.39E-11	3.18E-12	202.84	223
00035009185	WT	4604.37	57,066.09	2.46	0.04	7.65E-03	1.89E-04	3.72E-11	9.29E-13	484.02	501
00035009186	WT	4470.44	57,066.10	2.47	0.05	7.80E-03	2.06E-04	3.78E-11	1.01E-12	463.70	486
00035009187	WT	998.11	57,068.29	2.55	0.10	6.77E-03	3.98E-04	3.27E-11	1.92E-12	225.36	273
00035009188	WT	831.23	57,068.82	2.66	0.15	4.39E-03	3.79E-04	2.12E-11	1.85E-12	186.74	212
00035009189	WT	1028.06	57,069.95	2.40	0.14	3.91E-03	3.16E-04	1.91E-11	1.60E-12	209.45	228
00035009190	PC	1475.90	57,067.91	2.34	0.10	7.71E-03	4.81E-04	3.81E-11	2.50E-12	218.48	243
00035009192	WT	1077.83	57,070.23	2.46	0.18	3.75E-03	3.81E-04	1.82E-11	1.88E-12	200.21	207
00035009193	WT	1097.78	57,070.75	2.37	0.14	3.48E-03	2.92E-04	1.71E-11	1.49E-12	202.51	228
00035009194	WT	878.14	57,071.09	2.47	0.14	4.06E-03	3.47E-04	1.97E-11	1.70E-12	181.57	222
00035009195	WT	1062.83	57,071.69	2.48	0.13	4.25E-03	3.23E-04	2.06E-11	1.58E-12	232.91	242
00035009196	PC	1018.89	57,072.01	2.28	0.13	4.08E-03	3.37E-04	2.05E-11	1.84E-12	147.91	189
00035009197	PC	476.99	57,072.75	2.21	0.17	3.95E-03	4.34E-04	2.02E-11	2.50E-12	108.49	145
00035009198	PC	1016.40	57,073.01	2.31	0.12	4.28E-03	3.40E-04	2.13E-11	1.81E-12	136.03	198
00035009199	PC	1111.29	57,073.61	2.18	0.10	4.15E-03	2.85E-04	2.14E-11	1.68E-12	223.43	237
00035009200	PC	1016.40	57,074.14	2.19	0.12	3.53E-03	2.75E-04	1.82E-11	1.62E-12	210.63	208
00035009201	PC	1073.83	57,074.61	2.17	0.14	2.83E-03	2.59E-04	1.47E-11	1.55E-12	149.23	175

Note. Col. (1): the observation ID (ObsID). Col. (2): the readout mode, PC represents the photon counting mode, and WT represents the windowed timing mode. Col. (3): the net exposure time of Swift-XRT in units of second. Col. (4): the start time (MJD) of the Swift observation. Col. (5): the Swift-XRT photon index. Col. (6): the error of Swift-XRT photon index. Col. (7): the normalization flux in units of $cm^{-2}\ s^{-1}\ keV^{-1}$. Col. (8): the error of normalization flux in units of $cm^{-2}\ s^{-1}\ keV^{-1}$. Col. (9): the unabsorbed flux in 0.3−10 keV in units of ergs per square centimeter per second. Col. (10): the error of the unabsorbed flux in 0.3−10 keV in units of ergs per square centimeter per second. Col. (11): the Cash statistic. Col. (12): the degrees of freedom (d.o.f.).

Table 4
Swift-UVOT Aperture Photometric Data

	u Band			*b* Band			*v* Band			*uvw*1 Band			*uvw*2 Band			*uvm*2 Band		
ObsID (1)	MJD (2)	F_λ (3)	$F_{\lambda,\,\mathrm{err}}$ (4)	MJD (5)	F_λ (6)	$F_{\lambda,\,\mathrm{err}}$ (7)	MJD (8)	F_λ (9)	$F_{\lambda,\,\mathrm{err}}$ (10)	MJD (11)	F_λ (12)	$F_{\lambda,\,\mathrm{err}}$ (13)	MJD (14)	F_λ (15)	$F_{\lambda,\,\mathrm{err}}$ (16)	MJD (17)	F_λ (18)	$F_{\lambda,\,\mathrm{err}}$ (19)
00035009143	57011.04	1.12E-14	4.18E-16	57011.04	1.00E-14	3.23E-16	57011.04	8.32E-15	2.87E-16	57011.04	1.30E-14	6.43E-16	57011.04	1.57E-14	6.72E-16	57011.05	1.49E-14	6.08E-16
00035009144	57019.36	1.24E-14	4.51E-16	57019.36	1.07E-14	3.36E-16	57019.36	8.82E-15	2.90E-16	57019.36	1.33E-14	6.51E-16	57019.36	1.61E-14	6.84E-16	57019.37	1.56E-14	6.19E-16
00035009145	57023.22	1.04E-14	3.84E-16	57023.22	8.71E-15	2.79E-16	57023.22	7.52E-15	2.56E-16	57023.22	1.13E-14	5.58E-16	57023.22	1.41E-14	6.05E-16	57023.23	1.37E-14	5.50E-16
00035009146	57029.01	1.30E-14	4.83E-16	57029.01	1.16E-14	3.75E-16	57029.01	9.70E-15	3.33E-16	57029.01	1.42E-14	7.03E-16	57029.01	1.79E-14	7.69E-16	57029.01	1.77E-14	7.10E-16
00035009147	57041.09	6.36E-14	2.35E-15	57041.09	5.42E-14	1.73E-15	57041.10	5.05E-14	1.40E-15	57041.09	8.53E-14	4.00E-15	57041.10	1.09E-13	4.46E-15	57041.10	1.08E-13	3.94E-15
00035009148	57042.75	5.32E-14	1.89E-15	57042.75	4.46E-14	1.35E-15	57042.76	3.93E-14	1.07E-15	57042.75	6.22E-14	2.91E-15	57042.76	7.64E-14	3.13E-15	57042.76	7.60E-14	2.77E-15
00035009149	...	...	...	...	...	...	...	...	...	...	...	...	...	...	...	...	...	...
00035009152	57044.08	4.95E-14	1.77E-15	57044.08	4.05E-14	1.23E-15	57044.09	3.60E-14	9.96E-16	57044.08	5.96E-14	2.80E-15	57044.09	7.40E-14	3.04E-15	57044.09	7.46E-14	2.72E-15
00035009153	57044.29	4.55E-14	1.50E-15	...	...	...	...	...	...	...	...	...	...	...	...	...	...	...
	57044.36	4.51E-14	1.47E-15	...	...	...	...	...	...	...	...	...	...	...	...	...	...	...
	57044.42	4.61E-14	1.50E-15	...	...	...	...	...	...	...	...	...	...	...	...	...	...	...
	57044.48	4.95E-14	1.63E-15	...	...	...	...	...	...	...	...	...	...	...	...	...	...	...
	57044.55	5.18E-14	1.68E-15	...	...	...	...	...	...	...	...	...	...	...	...	...	...	...
	57044.62	5.33E-14	1.74E-15	...	...	...	...	...	...	...	...	...	...	...	...	...	...	...
	57044.68	5.29E-14	1.72E-15	...	...	...	...	...	...	...	...	...	...	...	...	...	...	...
	57044.81	5.61E-14	1.84E-15	...	...	...	...	...	...	...	...	...	...	...	...	...	...	...
	57044.95	6.02E-14	1.97E-15	...	...	...	...	...	...	...	...	...	...	...	...	...	...	...
00035009154	57045.01	5.76E-14	2.05E-15	57045.01	4.89E-14	1.48E-15	57045.02	4.43E-14	1.19E-15	57045.01	7.69E-14	3.59E-15	57045.02	1.00E-13	4.09E-15	57045.02	9.95E-14	3.60E-15
00035009156	...	...	...	...	...	...	...	...	...	...	...	...	57045.15	1.03E-13	4.18E-15	57046.15	1.28E-13	4.56E-15
	...	...	...	...	...	...	...	...	...	...	...	...	57045.28	1.05E-13	4.27E-15	57046.22	1.19E-13	4.25E-15
	...	...	...	...	...	...	...	...	...	...	...	...	57045.41	1.16E-13	4.71E-15	57046.28	1.10E-13	3.90E-15
	...	...	...	...	...	...	...	...	...	...	...	...	57045.48	1.18E-13	4.76E-15	57046.40	1.19E-13	4.32E-15
	...	...	...	...	...	...	...	...	...	...	...	...	57045.68	1.24E-13	5.03E-15	57046.48	1.14E-13	4.03E-15
00035009157	57047.14	7.07E-14	2.79E-15	57047.14	5.96E-14	2.05E-15	57047.14	5.67E-14	1.65E-15	57047.14	9.90E-14	4.68E-15	57047.48	1.13E-13	4.62E-15	57047.48	1.10E-13	3.98E-15
	57047.48	6.44E-14	2.40E-15	57047.48	5.44E-14	1.75E-15	57047.48	4.84E-14	1.36E-15	...	...	...	...	...	...	...	...	...
00035009158	...	...	...	...	...	...	...	...	...	57047.22	1.10E-13	5.07E-15	...	...	...	...	...	...
	...	...	...	...	...	...	...	...	...	57047.42	8.51E-14	3.91E-15	...	...	...	...	...	...
	...	...	...	...	...	...	...	...	...	57047.47	8.72E-14	4.10E-15	...	...	...	...	...	...
	...	...	...	...	...	...	...	...	...	57047.61	9.68E-14	4.45E-15	...	...	...	...	...	...
	...	...	...	...	...	...	...	...	...	57047.67	1.00E-13	4.61E-15	...	...	...	...	...	...
	...	...	...	...	...	...	...	...	...	57047.80	9.43E-14	4.35E-15	...	...	...	...	...	...
	...	...	...	...	...	...	...	...	...	57047.87	8.45E-14	3.88E-15	...	...	...	...	...	...
	...	...	...	...	...	...	...	...	...	57047.93	8.22E-14	3.79E-15	...	...	...	...	...	...
00035009159	57048.73	6.38E-14	2.36E-15	57048.73	5.19E-14	1.64E-15	57048.73	4.70E-14	1.30E-15	57048.73	8.48E-14	3.98E-15	57048.73	1.09E-13	4.47E-15	57048.74	1.08E-13	3.84E-15
00035009160	57048.87	6.49E-14	2.11E-15	...	...	...	...	...	...	...	...	...	...	...	...	...	...	...
00035009161	...	...	...	...	...	...	...	...	...	...	...	...	...	...	...	...	...	...
00035009162	57050.01	4.95E-14	1.92E-15	57050.01	4.22E-14	1.44E-15	57050.01	3.65E-14	1.14E-15	...	...	...	...	...	...	...	...	...
	57050.14	4.41E-14	1.70E-15	57050.14	3.58E-14	1.20E-15	57050.15	3.14E-14	9.95E-16	...	...	...	...	...	...	...	...	...
00035009167	57051.26	3.56E-14	1.36E-15	57051.32	3.05E-14	9.21E-16	57051.33	2.63E-14	7.49E-16	57051.26	4.23E-14	2.00E-15	57051.33	5.34E-14	2.20E-15	57051.33	5.21E-14	1.86E-15
	57051.32	3.56E-14	1.26E-15	57051.39	2.94E-14	8.88E-16	57051.40	2.47E-14	7.06E-16	57051.32	4.28E-14	2.02E-15	57051.39	5.12E-14	2.11E-15	57051.40	5.45E-14	6.72E-15
	57051.39	3.52E-14	1.24E-15	57051.46	2.75E-14	8.31E-16	...	...	...	57051.39	4.11E-14	1.94E-15	57051.46	4.82E-14	2.01E-15	...	...	...
	57051.46	3.31E-14	1.17E-15	...	...	...	...	...	...	57051.45	3.82E-14	1.81E-15	...	...	...	...	...	...
00035009164	57051.67	3.52E-14	1.32E-15	...	...	...	...	...	...	57051.66	4.13E-14	1.95E-15	...	...	...	...	...	...
00035009168	57051.93	3.36E-14	1.19E-15	57051.86	2.83E-14	8.54E-16	57051.86	2.40E-14	6.87E-16	57051.92	3.78E-14	1.79E-15	57051.93	4.65E-14	1.92E-15	...	...	...
	57051.95	3.30E-14	1.17E-15	57051.93	2.77E-14	8.35E-16	57051.93	2.37E-14	6.97E-16	57051.95	3.83E-14	1.81E-15	...	...	...	...	...	...
	57051.99	3.06E-14	1.08E-15	57051.99	2.66E-14	8.04E-16	...	...	...	...	...	...	...	...	...	...	...	...
00035009169	57052.27	3.04E-14	9.93E-16	57052.79	3.01E-14	8.60E-16	57052.80	2.65E-14	6.96E-16	...	...	...	...	...	...	...	...	...
	57052.79	3.47E-14	1.18E-15	...	...	...	...	...	...	...	...	...	...	...	...	...	...	...
	57052.86	3.54E-14	1.15E-15	...	...	...	...	...	...	...	...	...	...	...	...	...	...	...
	57052.99	3.28E-14	1.08E-15	...	...	...	...	...	...	...	...	...	...	...	...	...	...	...
00035009170	57053.00	3.20E-14	1.04E-15	57053.73	2.22E-14	6.58E-16	57053.73	1.88E-14	5.34E-16	...	...	...	57053.07	4.79E-14	1.95E-15	...	...	...
	57053.73	2.62E-14	9.14E-16	...	...	...	...	...	...	...	...	...	57053.14	4.21E-14	1.71E-15	...	...	...
	...	...	...	...	...	...	...	...	...	...	...	...	57053.20	4.19E-14	1.70E-15	...	...	...
	...	...	...	...	...	...	...	...	...	...	...	...	57053.54	4.15E-14	1.70E-15	...	...	...

Table 4
(Continued)

ObsID	*u* Band			*b* Band			*v* Band			*uvw*1 Band			*uvw*2 Band			*uvm*2 Band		
(1)	MJD (2)	F_λ (3)	$F_{\lambda,\ \mathrm{err}}$ (4)	MJD (5)	F_λ (6)	$F_{\lambda,\ \mathrm{err}}$ (7)	MJD (8)	F_λ (9)	$F_{\lambda,\ \mathrm{err}}$ (10)	MJD (11)	F_λ (12)	$F_{\lambda,\ \mathrm{err}}$ (13)	MJD (14)	F_λ (15)	$F_{\lambda,\ \mathrm{err}}$ (16)	MJD (17)	F_λ (18)	$F_{\lambda,\ \mathrm{err}}$ (19)
00035009171	57054.65	2.78E-14	9.48E-16	57054.65	2.34E-14	6.72E-16	57054.66	1.94E-14	5.24E-16	57054.65	3.29E-14	1.54E-15	57054.66	4.03E-14	1.65E-15	57054.59	4.04E-14	1.44E-15
	...	...	...	...	...	...	...	...	...	...	...	...	...	...	...	57054.66	3.92E-14	1.44E-15
00035009172	57055.45	3.59E-14	1.27E-15	57055.45	2.93E-14	8.80E-16	57055.46	2.44E-14	6.94E-16	57055.45	4.15E-14	1.96E-15	57055.45	5.20E-14	2.14E-15	57055.46	5.03E-14	1.85E-15
00035009173	57056.31	4.42E-14	1.58E-15	57056.31	3.54E-14	1.08E-15	57056.32	3.09E-14	8.71E-16	57056.31	5.44E-14	2.56E-15	57056.32	6.94E-14	2.85E-15	57056.32	6.80E-14	2.47E-15
00035009174	57057.64	4.21E-14	1.50E-15	57057.64	3.54E-14	1.08E-15	57057.65	2.90E-14	8.17E-16	...	...	...	57057.64	6.85E-14	2.81E-15	57057.65	6.69E-14	2.39E-15
00035009175	57058.52	4.43E-14	1.60E-15	57058.52	3.68E-14	1.13E-15	57058.53	3.06E-14	8.75E-16	57058.52	5.50E-14	2.59E-15	57058.52	7.11E-14	2.93E-15	57058.53	6.94E-14	2.53E-15
	57058.59	4.37E-14	1.54E-15	57058.59	3.52E-14	1.06E-15	57058.59	2.98E-14	8.29E-16	57058.59	5.48E-14	2.57E-15	57058.59	7.00E-14	2.87E-15	57058.60	6.79E-14	2.47E-15
00035009176	...	...	...	...	...	...	...	...	...	...	...	...	...	...	...	...	...	...
00035009177	57059.65	3.99E-14	1.36E-15	57059.65	3.28E-14	9.44E-16	57059.66	2.75E-14	7.44E-16	57059.05	5.07E-14	2.34E-15	57059.65	6.26E-14	2.55E-15	...	...	...
	...	...	...	...	...	...	...	...	...	57059.12	5.29E-14	2.43E-15	...	...	...	...	...	...
	...	...	...	...	...	...	...	...	...	57059.19	5.23E-14	2.40E-15	...	...	...	...	...	...
	...	...	...	...	...	...	...	...	...	57059.31	5.20E-14	2.39E-15	...	...	...	...	...	...
	...	...	...	...	...	...	...	...	...	57059.52	5.27E-14	2.43E-15	...	...	...	...	...	...
	...	...	...	...	...	...	...	...	...	57059.58	5.24E-14	2.41E-15	...	...	...	...	...	...
	...	...	...	...	...	...	...	...	...	57059.64	4.90E-14	2.28E-15	...	...	...	...	...	...
	...	...	...	...	...	...	...	...	...	57059.71	4.55E-14	2.10E-15	...	...	...	...	...	...
	...	...	...	...	...	...	...	...	...	57059.85	4.60E-14	2.11E-15	...	...	...	...	...	...
	...	...	...	...	...	...	...	...	...	57059.92	4.54E-14	2.09E-15	...	...	...	...	...	...
	...	...	...	...	...	...	...	...	...	57059.98	4.54E-14	2.09E-15	...	...	...	...	...	...
00035009178	57060.05	3.65E-14	1.20E-15	57060.98	2.87E-14	8.23E-16	57060.99	2.34E-14	6.24E-16	57060.98	4.22E-14	1.97E-15	57060.98	5.31E-14	2.17E-15	57060.99	5.06E-14	1.84E-15
	57060.12	3.79E-14	1.24E-15	...	...	...	...	...	...	...	...	...	...	...	...	...	...	...
	57060.19	3.97E-14	1.29E-15	...	...	...	...	...	...	...	...	...	...	...	...	...	...	...
	57060.25	3.83E-14	1.24E-15	...	...	...	...	...	...	...	...	...	...	...	...	...	...	...
	57060.32	3.83E-14	1.24E-15	...	...	...	...	...	...	...	...	...	...	...	...	...	...	...
	57060.39	3.85E-14	1.25E-15	...	...	...	...	...	...	...	...	...	...	...	...	...	...	...
	57060.52	3.63E-14	1.18E-15	...	...	...	...	...	...	...	...	...	...	...	...	...	...	...
	57060.58	3.51E-14	1.14E-15	...	...	...	...	...	...	...	...	...	...	...	...	...	...	...
	57060.72	3.47E-14	1.13E-15	...	...	...	...	...	...	...	...	...	...	...	...	...	...	...
	57060.79	3.48E-14	1.15E-15	...	...	...	...	...	...	...	...	...	...	...	...	...	...	...
	57060.86	3.41E-14	1.12E-15	...	...	...	...	...	...	...	...	...	...	...	...	...	...	...
	57060.91	3.41E-14	1.10E-15	...	...	...	...	...	...	...	...	...	...	...	...	...	...	...
	57060.98	3.43E-14	1.17E-15	...	...	...	...	...	...	...	...	...	...	...	...	...	...	...
00035009179	57061.24	3.21E-14	1.09E-15	57061.24	2.72E-14	7.78E-16	57061.25	2.24E-14	5.98E-16	57061.23	3.95E-14	1.84E-15	57061.05	5.53E-14	2.24E-15	57061.25	4.83E-14	1.75E-15
	...	...	...	...	...	...	...	...	...	...	...	...	57061.12	5.29E-14	2.14E-15	...	...	...
	...	...	...	...	...	...	...	...	...	...	...	...	57061.24	4.97E-14	2.03E-15	...	...	...
	...	...	...	...	...	...	...	...	...	...	...	...	57061.52	4.00E-14	1.62E-15	...	...	...
	...	...	...	...	...	...	...	...	...	...	...	...	57061.57	4.20E-14	1.73E-15	...	...	...
	...	...	...	...	...	...	...	...	...	...	...	...	57061.78	4.77E-14	1.93E-15	...	...	...
00035009180	...	...	...	...	...	...	...	...	...	...	...	...	...	...	...	57062.06	3.84E-14	1.44E-15
	...	...	...	...	...	...	...	...	...	...	...	...	...	...	...	57062.17	3.90E-14	1.39E-15
	...	...	...	...	...	...	...	...	...	...	...	...	...	...	...	57062.24	4.26E-14	1.52E-15
	...	...	...	...	...	...	...	...	...	...	...	...	...	...	...	57062.31	4.11E-14	1.47E-15
	...	...	...	...	...	...	...	...	...	...	...	...	...	...	...	57062.37	4.03E-14	1.48E-15
	...	...	...	...	...	...	...	...	...	...	...	...	...	...	...	57062.44	3.91E-14	1.39E-15
	...	...	...	...	...	...	...	...	...	...	...	...	...	...	...	57062.50	3.84E-14	1.37E-15
	...	...	...	...	...	...	...	...	...	...	...	...	...	...	...	57062.57	3.85E-14	1.37E-15
	...	...	...	...	...	...	...	...	...	...	...	...	...	...	...	57062.64	3.75E-14	1.34E-15
	...	...	...	...	...	...	...	...	...	...	...	...	...	...	...	57062.70	3.71E-14	1.32E-15
00035009181	57063.96	2.46E-14	8.60E-16	57063.96	2.08E-14	6.22E-16	57063.97	1.75E-14	5.07E-16	57063.96	2.94E-14	1.39E-15	57063.97	3.74E-14	1.54E-15	57063.97	3.68E-14	1.38E-15
00035009182	57064.30	2.59E-14	9.17E-16	57064.30	2.15E-14	6.54E-16	57064.31	1.80E-14	5.34E-16	57064.30	3.07E-14	1.46E-15	57064.31	3.92E-14	1.63E-15	57064.31	3.70E-14	1.39E-15
00035009184	57066.03	3.10E-14	1.09E-15	57066.04	2.44E-14	7.29E-16	...	...	...	57066.03	3.58E-14	1.69E-15	57066.04	4.68E-14	1.94E-15	57066.10	4.39E-14	1.57E-15
00035009185	...	...	...	...	...	...	...	...	...	...	...	...	...	...	...	57066.11	4.36E-14	1.56E-15
	...	...	...	...	...	...	...	...	...	...	...	...	...	...	...	57066.17	4.42E-14	1.58E-15
	...	...	...	...	...	...	...	...	...	...	...	...	...	...	...	57066.23	4.47E-14	1.60E-15

Table 4
(Continued)

ObsID	*u* Band			*b* Band			*v* Band			*uvw*1 Band			*uvw*2 Band			*uvm*2 Band		
(1)	MJD (2)	F_λ (3)	$F_{\lambda,\ \mathrm{err}}$ (4)	MJD (5)	F_λ (6)	$F_{\lambda,\ \mathrm{err}}$ (7)	MJD (8)	F_λ (9)	$F_{\lambda,\ \mathrm{err}}$ (10)	MJD (11)	F_λ (12)	$F_{\lambda,\ \mathrm{err}}$ (13)	MJD (14)	F_λ (15)	$F_{\lambda,\ \mathrm{err}}$ (16)	MJD (17)	F_λ (18)	$F_{\lambda,\ \mathrm{err}}$ (19)
	...	...	...	...	...	...	...	...	...	...	...	...	...	...	...	57066.24	4.40E-14	1.57E-15
	...	...	...	...	...	...	...	...	...	...	...	...	...	...	...	57066.30	4.22E-14	1.51E-15
	...	...	...	...	...	...	...	...	...	...	...	...	...	...	...	57066.31	4.27E-14	1.53E-15
	...	...	...	...	...	...	...	...	...	...	...	...	...	...	...	57066.36	4.34E-14	1.55E-15
00035009186	...	...	...	...	...	...	...	...	...	...	...	...	...	...	...	57066.37	4.40E-14	1.58E-15
00035009190	57067.91	3.06E-14	1.08E-15	57067.91	2.57E-14	7.75E-16	57067.97	2.09E-14	6.08E-16	57067.96	3.75E-14	1.77E-15	57067.97	4.91E-14	2.03E-15	...	...	...
	57067.97	3.12E-14	1.10E-15	57067.97	2.57E-14	7.75E-16	...	...	...	...	...	...	...	...	...	...	...	...
00035009187	57068.30	2.77E-14	9.63E-16	...	...	...	...	...	...	57068.30	3.36E-14	1.58E-15	57068.30	4.24E-14	1.75E-15	57068.29	4.17E-14	1.54E-15
00035009188	...	...	...	...	...	...	...	...	...	57068.82	2.59E-14	1.24E-15	57068.83	3.22E-14	1.34E-15	57068.82	3.11E-14	1.18E-15
00035009189	57069.96	2.04E-14	7.10E-16	...	...	...	...	...	...	57069.96	2.42E-14	1.14E-15	57069.96	2.98E-14	1.24E-15	...	...	...
00035009192	57070.23	2.02E-14	7.01E-16	...	...	...	...	...	...	57070.23	2.32E-14	1.10E-15	57070.24	2.87E-14	1.19E-15	57070.23	2.86E-14	1.07E-15
00035009193	57070.76	1.77E-14	6.16E-16	...	...	...	...	...	...	57070.76	2.00E-14	9.51E-16	57070.76	2.51E-14	1.04E-15	...	...	...
00035009194	57071.09	2.01E-14	7.11E-16	...	...	...	...	...	...	57071.09	2.36E-14	1.12E-15	57071.10	3.06E-14	1.27E-15	57071.09	2.95E-14	1.12E-15
00035009195	57071.69	2.17E-14	7.58E-16	...	...	...	...	...	...	57071.69	2.44E-14	1.15E-15	57071.70	3.14E-14	1.30E-15	57071.69	3.00E-14	1.12E-15
00035009196	57072.02	2.17E-14	7.61E-16	...	...	...	...	...	...	57072.02	2.52E-14	1.20E-15	57072.02	3.15E-14	1.30E-15	57072.75	3.80E-14	1.50E-15
00035009197	57072.75	2.69E-14	1.02E-15	...	...	...	...	...	...	57072.75	3.06E-14	1.49E-15	57072.75	3.95E-14	1.66E-15	...	...	...
00035009198	57073.02	2.27E-14	7.93E-16	...	...	...	...	...	...	57073.01	2.69E-14	1.27E-15	57073.02	3.43E-14	1.41E-15	57073.01	3.33E-14	1.24E-15
00035009199	57073.61	2.14E-14	7.50E-16	...	...	...	...	...	...	57073.61	2.39E-14	1.13E-15	57073.62	3.13E-14	1.29E-15	57073.61	3.01E-14	1.13E-15
00035009200	57074.15	1.65E-14	5.84E-16	...	...	...	...	...	...	57074.15	1.93E-14	9.20E-16	57074.15	2.38E-14	9.91E-16	57074.14	2.35E-14	8.94E-16
00035009201	57074.61	1.46E-14	5.19E-16	...	...	...	...	...	...	57074.61	1.71E-14	8.21E-16	57074.62	2.17E-14	9.05E-16	57074.61	2.12E-14	8.09E-16

Note. Observation ID (ObsID). These optical fluxes are corrected for the Galactic extinction. The units of F_λ is erg cm^{-2} s^{-1} Å^{-1}. The symbol "..." represents a null value.

ORCID iDs

Zhihao Ouyang https://orcid.org/0009-0000-4102-9115
Hubing Xiao https://orcid.org/0000-0001-8244-1229
Marina Manganaro https://orcid.org/0000-0003-1530-3031
Rui Xue https://orcid.org/0000-0003-1721-151X
Gege Wang https://orcid.org/0000-0002-8032-4640
Shaohua Zhang https://orcid.org/0000-0001-8485-2814
Junhui Fan https://orcid.org/0000-0002-5929-0968

References

Abdo, A. A., Ackermann, M., Ajello, M., et al. 2010, ApJ, 722, 520
Abdollahi, S., Acero, F., Baldini, L., et al. 2022, ApJS, 260, 53
Aharonian, F., Akhperjanian, A. G., Bazer-Bachi, A. R., et al. 2007, ApJL, 664, L71
Ajello, M., Atwood, W. B., Axelsson, M., et al. 2021, ApJS, 256, 12
Albert, J., Aliu, E., Anderhub, H., et al. 2007, ApJ, 669, 862
Anderhub, H., Antonelli, L. A., Antoranz, P., et al. 2009, ApJL, 704, L129
Atwood, W. B., Abdo, A. A., Ackermann, M., et al. 2009, ApJ, 697, 1071
Bach, U., Krichbaum, T. P., Ros, E., et al. 2005, A&A, 433, 815
Bachev, R., Spassov, B., & Boeva, S. 2015, ATel, 6944, 1
Bachev, R., & Strigachev, A. 2015, ATel, 6957, 1
Banik, P., & Bhadra, A. 2019, PhRvD, 99, 103006
Banik, P., Bhadra, A., Pandey, M., & Majumdar, D. 2020, PhRvD, 101, 063024
Barthelmy, S. D., Barbier, L. M., Cummings, J. R., et al. 2005, SSRv, 120, 143
Błażejowski, M., Sikora, M., Moderski, R., & Madejski, G. M. 2000, ApJ, 545, 107
Böttcher, M., Reimer, A., & Marscher, A. P. 2009, ApJ, 703, 1168
Breeveld, A. A., Curran, P. A., Hoversten, E. A., et al. 2010, MNRAS, 406, 1687
Breeveld, A. A., Landsman, W., Holland, S. T., et al. 2011, in AIP Conf. Ser. 1358, Gamma Ray Bursts 2010, ed. J. E. McEnery, J. L. Racusin, & N. Gehrels (Melville, NY: AIP), 373
Burrows, D. N., Hill, J. E., Nousek, J. A., et al. 2004, Proc. SPIE, 5165, 201
Cappi, M., Comastri, A., Molendi, S., et al. 1994, MNRAS, 271, 438
Carrasco, L., Porras, A., Recillas, E., et al. 2015, ATel, 6902, 1
Carver, T. 2019, ICRC, 36, 851
Cash, W. 1979, ApJ, 228, 939
Cerruti, M., Zech, A., Boisson, C., et al. 2019, MNRAS, 483, L12
Cerruti, M., Zech, A., Boisson, C., & Inoue, S. 2015, MNRAS, 448, 910
Chandra, S., Zhang, H., Kushwaha, P., et al. 2015, ApJ, 809, 130
Cleary, K., Lawrence, C. R., Marshall, J. A., Hao, L., & Meier, D. 2007, ApJ, 660, 117
Dai, B.-z., Zeng, W., Jiang, Z.-j., et al. 2015, ApJS, 218, 18
Danforth, C. W., Nalewajko, K., France, K., & Keeney, B. A. 2013, ApJ, 764, 57
Dermer, C. D., & Schlickeiser, R. 1993, ApJ, 416, 458
Domìnguez, A., Primack, J. R., Rosario, D. J., et al. 2011, MNRAS, 410, 2556
Edelson, R. A., & Krolik, J. H. 1988, ApJ, 333, 646
Fan, J.-H., Wang, Y.-J., Yang, J.-H., & Su, C.-Y. 2004, ChJAA, 4, 533
Fan, J. H., Yang, J. H., Liu, Y., et al. 2016, ApJS, 226, 20
Fermi Science Support Development Team, 2019 Fermitools: Fermi Science Tools, Astrophysics Source Code Library, ascl:1905.011
Finke, J. D., Dermer, C. D., & Böttcher, M. 2008, ApJ, 686, 181
Fitzpatrick, E. L. 1999, PASP, 111, 63
Foschini, L., Tagliaferri, G., Pian, E., et al. 2006, A&A, 455, 871
Gao, S., Fedynitch, A., Winter, W., & Pohl, M. 2019, NatAs, 3, 88
Gasparyan, S., Sahakyan, N., Baghmanyan, V., & Zargaryan, D. 2018, ApJ, 863, 114
Gehrels, N., Chincarini, G., Giommi, P., et al. 2004, ApJ, 611, 1005
Geng, X., Zeng, W., Rani, B., et al. 2020, ApJ, 904, 67
Ghiassi, K., & Salwén, J. 2023Student Thesis, KTH, School of Engineering Sciences
Ghisellini, G., & Tavecchio, F. 2009, MNRAS, 397, 985
Ghisellini, G., Tavecchio, F., Foschini, L., et al. 2010, MNRAS, 402, 497
Giannios, D., Uzdensky, D. A., & Begelman, M. C. 2009, MNRAS, 395, L29
Giannios, D., Uzdensky, D. A., & Begelman, M. C. 2010, MNRAS, 402, 1649
Gupta, A. C., Krichbaum, T. P., Wiita, P. J., et al. 2012, MNRAS, 425, 1357
Harrison, F. A., Craig, W. W., Christensen, F. E., et al. 2013, ApJ, 770, 103
Hartman, R. C., Bertsch, D. L., Bloom, S. D., et al. 1999, ApJS, 123, 79
HI4PI Collaboration, Ben Bekhti, N., Flöer, L., et al. 2016, A&A, 594, A116
Ikejiri, Y., Uemura, M., Sasada, M., et al. 2011, PASJ, 63, 639
Kaspi, S., Brandt, W. N., Maoz, D., et al. 2007, ApJ, 659, 997
Kelner, S. R., Aharonian, F. A., & Bugayov, V. V. 2006, PhRvD, 74, 034018
Kraus, A., Krichbaum, T. P., Wegner, R., et al. 2003, A&A, 401, 161
Kuehr, H., Witzel, A., Pauliny-Toth, I. I. K., & Nauber, U. 1981, A&AS, 45, 367
Li, W.-J., Xue, R., Long, G.-B., et al. 2022, A&A, 659, A184
Liao, N. H., Bai, J. M., Liu, H. T., et al. 2014, ApJ, 783, 83
Lin, Y. C., Bertsch, D. L., Dingus, B. L., et al. 1995, ApJ, 442, 96
Lister, M. L., Aller, M. F., Aller, H. D., et al. 2018, ApJS, 234, 12
Lister, M. L., Homan, D. C., Hovatta, T., et al. 2019, ApJ, 874, 43
Liu, H. T., Feng, H. C., Xin, Y. X., et al. 2019, ApJ, 880, 155
Liu, R.-Y., Wang, K., Xue, R., et al. 2019, PhRvD, 99, 063008
Lyutikov, M., & Kravchenko, E. V. 2017, MNRAS, 467, 3876
MAGIC Collaboration, Ahnen, M. L., Ansoldi, S., et al. 2018, A&A, 619, A45
Mirzoyan, R. 2015, ATel, 6999, 1
Morrison, R., & McCammon, D. 1983, ApJ, 270, 119
Mücke, A., Protheroe, R. J., Engel, R., Rachen, J. P., & Stanev, T. 2003, APh, 18, 593
Nolan, P. L., Abdo, A. A., Ackermann, M., et al. 2012, ApJS, 199, 31
Perley, R. A., Fomalont, E. B., & Johnston, K. 1980, AJ, 85, 649
Pichel, A., Donzelli, C., Muriel, H., et al. 2023, A&A, 680, A52
Poole, T. S., Breeveld, A. A., Page, M. J., et al. 2008, MNRAS, 383, 627
Poon, H., Fan, J. H., & Fu, J. N. 2009, ApJS, 185, 511
Rani, B., Krichbaum, T. P., Fuhrmann, L., et al. 2013a, A&A, 552, A11
Rani, B., Krichbaum, T. P., Marscher, A. P., et al. 2015, A&A, 578, A123
Rani, B., Krichbaum, T. P., Marscher, A. P., et al. 2014, A&A, 571, L2
Rani, B., Lott, B., Krichbaum, T. P., Fuhrmann, L., & Zensus, J. A. 2013b, A&A, 557, A71
Roming, P. W. A., Kennedy, T. E., Mason, K. O., et al. 2005, SSRv, 120, 95
Roy, N., Chatterjee, R., Joshi, M., & Ghosh, A. 2019, MNRAS, 482, 743
Scarpa, R., & Falomo, R. 1997, A&A, 325, 109
Schlafly, E. F., & Finkbeiner, D. P. 2011, ApJ, 737, 103
Shaw, M. S., Romani, R. W., Healey, S. E., et al. 2009, ApJ, 704, 477
Shukla, A., & Mannheim, K. 2020, NatCo, 11, 4176
Sikora, M., Begelman, M. C., & Rees, M. J. 1994, ApJ, 421, 153
Stickel, M., Padovani, P., Urry, C. M., Fried, J. W., & Kuehr, H. 1991, ApJ, 374, 431
Tagliaferri, G., Ravasio, M., Ghisellini, G., et al. 2003, A&A, 400, 477
Tan, C., Xue, R., Du, L.-M., et al. 2020, ApJS, 248, 27
Tavecchio, F., Maraschi, L., & Ghisellini, G. 1998, ApJ, 509, 608
Tramacere, A., 2020 JetSeT: Numerical Modeling and SED Fitting Tool for Relativistic Jets, Astrophysics Source Code Library, ascl:2009.001
Tramacere, A., Giommi, P., Perri, M., Verrecchia, F., & Tosti, G. 2009, A&A, 501, 879
Tramacere, A., Massaro, E., & Taylor, A. M. 2011, ApJ, 739, 66
Tripathi, T., Gupta, A. C., Takey, A., et al. 2024, MNRAS, 527, 5220
Urry, C. M., & Padovani, P. 1995, PASP, 107, 803
Verner, D. A., Ferland, G. J., Korista, K. T., & Yakovlev, D. G. 1996, ApJ, 465, 487
Wagner, S. J., Witzel, A., Heidt, J., et al. 1996, AJ, 111, 2187
Wang, G., Fan, J., Xiao, H., & Cai, J. 2022, PASP, 134, 104101
Wierzcholska, A., & Siejkowski, H. 2015, MNRAS, 452, L11
Wierzcholska, A., & Siejkowski, H. 2016, MNRAS, 458, 2350
Wilms, J., Allen, A., & McCray, R. 2000, ApJ, 542, 914
Wit, E., Heuvel, E. v. d., & Romeijn, J.-W. 2012, Stat. Neerl., 66, 217
Xiao, H., Fan, J., Yang, J., et al. 2019, SCPMA, 62, 129811
Xiao, H. B., Zhu, J. T., Fan, J. H., et al. 2022, MNRAS, 517, 4202
Xiong, D., Bai, J., Fan, J., et al. 2020, ApJS, 247, 49
Xue, R., Liu, R.-Y., Wang, X.-Y., Yan, H., & Böttcher, M. 2019, ApJ, 871, 81
Xue, R., Wang, Z.-R., & Li, W.-J. 2022, PhRvD, 106, 103021